INFN Istituto Nazionale di Fisica Nucleare

LABORATORI NAZIONALI DI FRASCATI
SIS – Pubblicazioni

LNF–08/ 22 (IR)
October 2, 2008

ON CRYSTAL-ASSISTED PROCESSES BY MEANS OF 20-800 MeV e^-/e^+ LNF BEAMS

A. Babaev[1], O.V. Bogdanov[1], V.I. Efremov[1], K.B. Korotchenko[1], Yu.P. Kunashenko[1], Yu.L. Pivovarov[1], and S.B. Dabagov[2,3]

[1] *Tomsk Polytechnic University, Tomsk (Russia)*
[2] *INFN Laboratori Nazionali di Frascati, Frascati (Italy)*
[3] *RAS P.N. Lebedev Physical Institute, Moscow (Russia)*

Abstract

Recently LNF INFN has started the research in developing novel powerful radiation sources such as synchrotron radiation sources, free electron lasers, electron/positron channeling in crystals, etc. This activity has resulted in the design of new beam lines at the DAFNE-L synchrotron radiation laboratory and the construction of a new facility SPARC based on FEL SASE phenomenon; channeling studies for relativistic positrons are presently performing at DAFNE BTF. In the nearest future LNF is going to launch a new project on electron/positron channeling phenomena.

Based on this idea, in this report we are discussing the features of 20-800 MeV e^-/e^+ channeling in various crystals. Namely, paying attention to the complex character of radiation origin, the new peculiarities of channeling radiation from relativistic particles have been described in details; the processes of multiple scattering have been studied using a modified binary collision model; the possibility of the particle spin manifestation in radiation parameters has been analyzed; various solutions for coherent production of e^-/e^+ pairs in crystals have been presented. The results of both computer simulations and estimations are given in many figures and tables.

PACS: 61.85.+p

1. COHERENT PRODUCTION OF FREE AND BOUND ELECTRON-POSITRON PAIRS BY PHOTONS AND CHARGED PARTICLES IN A CRYSTAL

1.1 Pioneering studies of e^+/e^- coherent photo-production and strong collimation effects for created pairs

After prediction of coherent bremsstrahlung (CB) and coherent pairs production (CPP) by Ter-Mikaelian [1.1] and Uberall [1.2], a very few experiments on CPP by photons have been performed. The 1st experiments at Frascati were carried out by Bologna, Diambrini, and Murtas.[1.3] They have resolved the expected central minimum in the electron pair production and found only a qualitative agreement with the theoretical results. The review of other experiments on CPP of type-A (revealed at a few GeV photon energies)[1] was given by Diambrini [1.4]; the further development of a CPP theory was done by Ter-Mikaelian [1.5]. After those publications, almost 20 years later, Cue and Kimball [1.6] considered a type-B CPP and have shown that the coherent effect for CPP in a crystal may take place even at the photon energy below 1 GeV. The first experiments [1.7,1.8] confirmed the existence of a type-B effect even with a small brilliance of the coherent peaks. The idea to increase the brilliance of coherent peaks in CPP using strong collimation of created particles, first suggested in [1.9-1.11], was realized in the experiments carried out at the INS Tokyo synchrotron (KEK) in 1998 [1.12,1.13]; a type-B CPP was observed when the incident photon momentum is parallel to a crystallographic axis. The detailed studies of the type-B CPP in thin crystals that reveals at photon energies below 1 GeV, can be the subject for experimental investigations using a bremsstrahlung beam (or even a tagged photon beam) at LNF (BTF, Frascati).

Using the equations for coherent production of e^+-e^- pairs under strong collimation of created particles [1.9-1.10], we carried out the calculations and present here the representative results for symmetric (equal-energy) pairs. As it is seen from Figures, the brilliance (the relation of coherent peak intensity to incoherent background) increases to 16 times in the last case, while collimation angle decreases from 10 mrad up to 1 mrad.

[1] Coherent process of a type A takes place when the initial photon momentum has small angle with respect to system of crystallographic planes, while coherent process of type B arises when initial photon momentum is parallel to crystal axis.

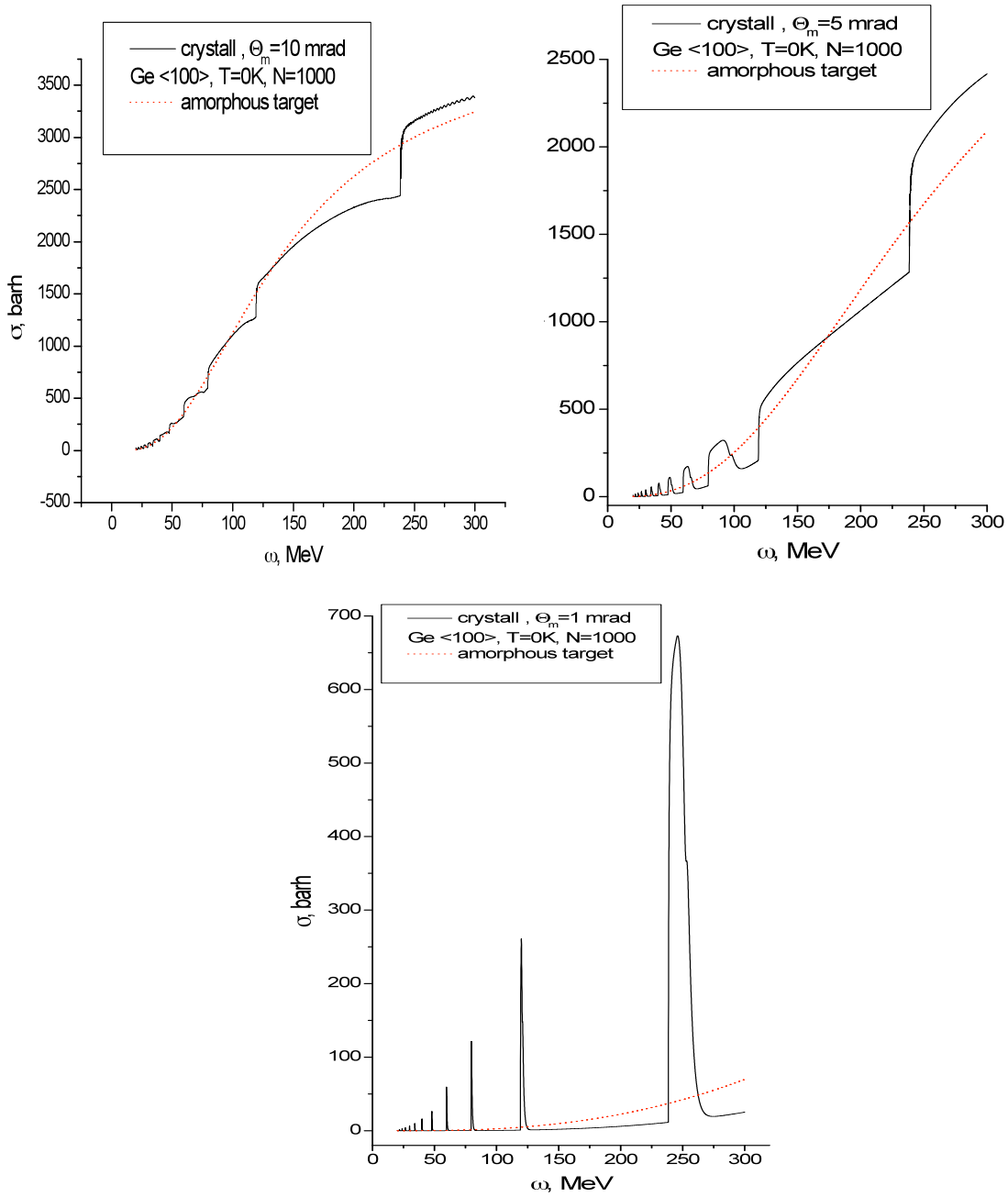

Figure 1.1. Type-B CPP: brilliance of coherent peaks by improving radiation collimation

1.2 From coherent photo-production of "narrow" e+/e- pairs to coherent photo-production of bound e+e- pairs. Ps atom moving with relativistic velocity

A special case in the pairs' production by high-energy photons relates to the production of bound electron and positron pair, i.e. a positronium atom moving with large velocity.

For the first time the possibility of positronium atom (Ps) creation by a photon in the atom field was considered in [1.14]; theory of relativistic Ps production in the first Born approximation (valid only for singlet Ps) was proposed by Olsen [1.15] and Luboshits [1.16]. The cross-sections for singlet and triplet Ps creation by relativistic electron in the Coulomb field was calculated by Holvik and Olsen [1.17]. Later theory of Ps production by photons and

electrons in the field of single atom was developed by Kuraev and co-authors [1.18-1.20] and, independently, by Olsen [1.21,1.22].

The possibility of coherent type B creation of Ps in a crystal was first predicted for both the photo-production [1.23] and production by relativistic electrons [1.24]. In [1.22-23] it was shown that the sharp coherent peaks appear at definite Ps energies and emission angles. Detailed theoretical investigations of Ps coherent type B photo-production and production by relativistic electrons in crystals have been performed in [1.23,1.24]. In [1.23-1.26] one string approximation was used taking into account interaction of incident photon (electron) with a single crystal axis (1D model); detailed theory of coherent type B Ps production by both a photon and a high energy electron in a real (3D model) crystal was considered in the first Born approximation [1.27]. Problems connected with slow and fast Ps atoms generation and its use were the subject of International Workshop "Hadronic atoms and positronium in the standard model" in Dubna (1998) [1.28].

What is the motivation to study experimentally the coherence effects in production of relativistic Ps atoms in crystals? First, new coherent effects in a crystal target predicted for a photon/electron beam of moderate energies (up to a few hundreds MeV) can be recorded, while the detection seems the worth challenge for experimentalists. A monochromatic beam of Ps atoms allows direct measurements of two-photon decay for a singlet Ps, and hence, studying a singlet Ps lifetime; presently these studies are based on the analysis of Ps stopping in matter when a real Ps wave function differs very much from a Ps wave function in a vacuum. Generation of Ps atoms due to photon/electron collisions with atoms (both in amorphous and crystal targets) is a higher order QED effect never observed before.

The differential over emission angles cross-section of the Ps production by a photon with energy ω in the Coulomb field of an atom is written as follows [1.15,1.16] ($\hbar$=c=1)

$$\frac{d\sigma_1^{ph}}{d\Omega} = \frac{Z^2\alpha^6}{8m^2\gamma^4}\frac{\sin^2\Theta}{\left(1-\beta^2-2\beta\cos\Theta\right)^2\left(1-\beta\cos\Theta\right)^2} \tag{1.1}$$

Here, α is the fine structure constant, γ and β are, respectively, the relativistic factor and velocity of created Ps, Θ is the Ps emission angle with respect to a photon momentum, m is the electron rest mass, Z is the target atomic number. The momentum transferred to atom is defined by

$$q^2 = \left(E^2 + p^2 - 2Ep\cos\Theta\right) = E^2\left(1-\beta^2-2\beta\cos\Theta\right),$$

where E ≡ ω and p are the Ps energy is momentum, correspondingly.

In a crystal, the cross-section of Ps photo-production is written [1.21,1.23] as the sum of coherent $d\sigma_{coh}$ and incoherent $d\sigma_{incoh}$ parts

$$d\sigma_{cr} = d\sigma_{coh} + d\sigma_{incoh}\ ,$$
$$d\sigma_{coh} = I\left(\vec{q}\right)\exp\left(-q^2\overline{u^2}\right)d\sigma_1; \qquad d\sigma_{incoh} = N\left[1-\exp\left(-q^2\overline{u^2}\right)\right]d\sigma_1. \tag{1.2}$$

Here, $\exp(-q^2\overline{u^2})$ is the Debye-Waller factor, which takes into account the thermal vibrations of the crystal atoms, $\overline{u^2}$ is the mean-squared deviation of a crystal atom from the equilibrium position, $I(\vec{q})$ is the interference term due to the coherence. In our case $I(\vec{q})$ is presented in the following

$$I(\vec{q}) = N_x N_y \frac{(2\pi)^2}{d_x d_y} \sum_{n,l} \delta(q_x - g_x n) \cdot \delta(q_y - g_y l) \cdot \frac{\sin^2(N_z q_z d_z/2)}{\sin^2(q_z d_z/2)} \cdot |S(\vec{q})|^2 \qquad (1.3)$$

In Eq.(1.3) $\{N_x,N_y,N_z\}$ are the numbers of crystal atoms in $\{x,y,z\}$ directions respectively, which contribute into coherent process; $g_x n = 2\pi n / d_x$, $g_y l = 2\pi l / d_y$, $_{n,l=1,2,3,...}$ are the components of reciprocal lattice vector $\vec{q}$ in x and y directions and $\{d_x,d_y,d_z\}$ are the lattice constant in $\{x,y,z\}$ directions, respectively; $S(\vec{q})$ is the crystal structure factor.

At LNF, we propose an experiment to measure the Ps yield within small angular cone.

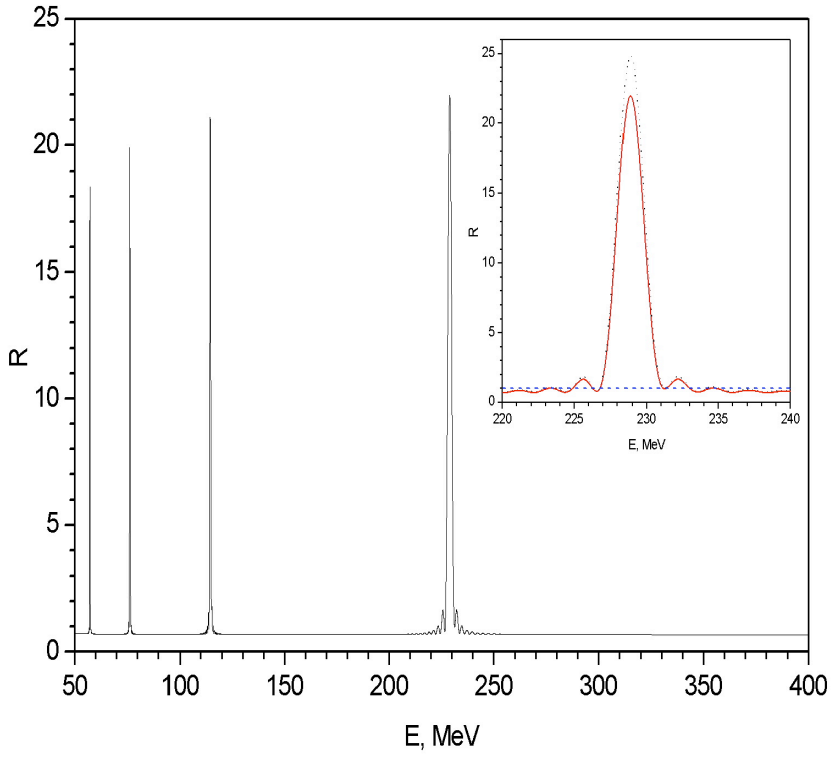

Figure 1.2. Coherent production of singlet Ps atom: enhancement *R* versus photon energy

In order to demonstrate the coherent effect it is convenient to introduce the ratio *R* of coherent type B production of Ps by high energy photon in a crystal to one in an amorphous target of equivalent thickness, which contains the same number N_z of atoms as a crystal:

$$R = \frac{\sigma_{cr}}{N\sigma_1} = \frac{\sigma_{coh} + \sigma_{incoh}}{\sigma_1}.$$

Fig. 1.2 shows the dependence of the ratio *R* on photon energy calculated for *Ge* crystal, oriented by axis <100> with respect to a photon momentum. The cross–sections of Ps photo-production in a crystal and in an amorphous target were integrated over the emission angles $\Theta = 0 \div \Theta_{max}$. The maximal emission angle of Ps was chosen to be Θ_{max}=5 mrad and the number of atoms in a crystal axis - N_z=100 (3D model).

The detailed structure of the coherent peak in the vicinity of the 1st coherent maximum near the photon energy $\omega \approx 229$ MeV is shown in the insertion to Fig. 1.2 (solid line). In order to compare the result of 3D and 1D models, the ratio R calculated within the framework of 1D-model is shown in Fig. 1.1b by dotted line. The dashed line shows the level $R = 1$. As follows from the insertion to Fig. 1.2, the calculated values of R according to 1D and 3D models are in a good agreement. It proves that, as it happens in a 1D-model, in the case of a 3D model a fine structure can be observed in the dependence of cross-section of coherent type-B Ps photo-production on incident photon energy.

1.3 Singlet Ps production by relativistic electrons

Both the triplet and singlet Ps can be also produced by relativistic electron passing through a crystal [1.22]. We restrict our consideration by only singlet Ps coherent production. In this case one can derive the cross-section in a frame of the virtual photon method [1.17,1.27]. The differential cross-section for electro-production in a crystal has the same form as given by Eqs.(1.2), where $d\sigma_1^{el}$ represents the electro-production cross-section of singlet Ps on an individual atom [1.17]

$$\frac{d\sigma_1^{el}}{d\Omega dE_{Ps}} = \frac{d\sigma_1^{ph}}{d\Omega}(\omega = E_{Ps}) \cdot n(E_{Ps}, E_1)$$

Here, $n(E_{Ps}, E_1)$ is the virtual photon spectrum associated with an incident relativistic electron

$$n(E_{Ps}, E_1) = \frac{\alpha}{2\pi} \frac{1}{E_{Ps}} \left\{ \left[1 + \left(\frac{E_1 - E_{Ps}}{E_1} \right)^2 \right] \ln \frac{E_1 (E_1 - E_{Ps})}{m_e^2 c^4 \gamma^2} - 2 \left(\frac{E_1 - E_{Ps}}{E_1} \right) \right\},$$

where E_1 is the initial electron energy, E_{Ps} is the singlet Ps atom energy. The cross-section $d\sigma_1^{ph}(\omega)$ is given by Eq.(1.1), therefore further investigation is straightforward.

The cross-sections of coherent type B production of Ps by relativistic electrons (lower part) and photon (upper part) versus Ps energy are plotted in Fig. 1.3. The incident electron beam energy is $E_1 = 500$ MeV. The cross-section is integrated over Ps emission angles assuming the maximum emission angle to be Θ_{max}=5 mrad. The number of atoms in a crystal axis is $N_z = 10^3$, the crystal temperature is $T = 0\ K$. Dotted lines show the cross-sections of Ps production by both electron ($\frac{d\sigma_1^{el}}{dE_1} = d\sigma_1^{ph}(\omega) \cdot n(\omega)$) and photon ($d\sigma_1^{ph}(\omega)$) in an amorphous

target of equivalent thickness, which contains the same number N of atoms as a crystal (Si <100>) .

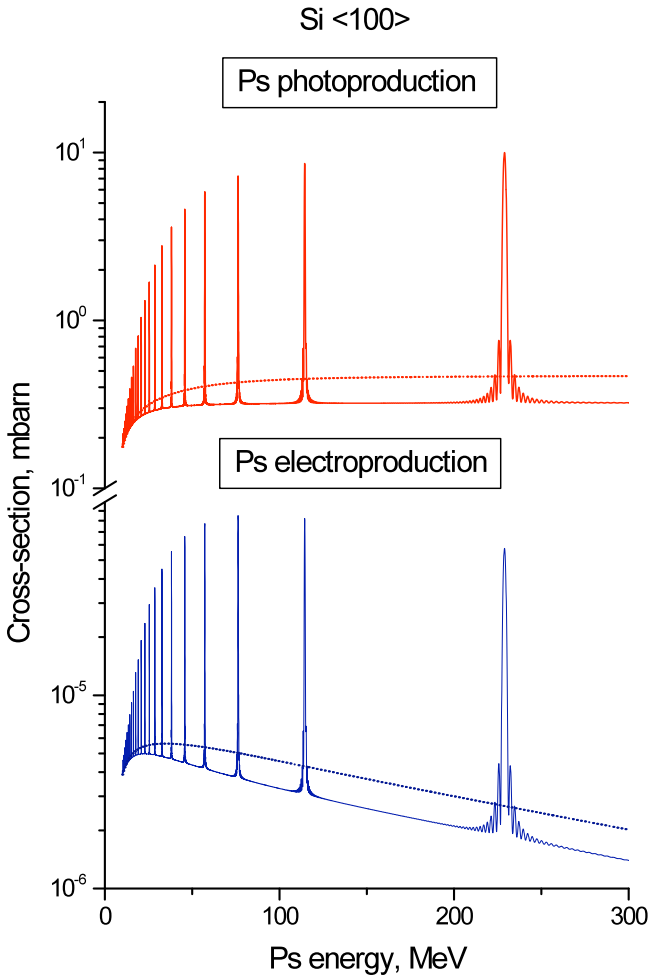

Figure 1.3. Coherent production of a Ps atom by both monochromatic photon (upper part) and electron beams (lower part). In the upper part, at fixed photon beam energy a monochromatic Ps beam is created, i.e. a photon energy is equal to a Ps atom energy. In lower part, at fixed electron beam energy one appears a broad energy spectrum of created Ps with well-pronounced coherent peaks.

The possible scheme of experimental setup (at REFER) to study these processes was discussed in [1.24], and it would be rather interesting to organize a set of experimental studies at accelerator facilities of LNF (BTF facility of DAFNE Linac for 100-800 MeVe^-/e^+ beams and SPARC facility for 150 MeV e^- beams; for detail characteristics of the beams see below).

2. NEW FEATURES OF CHANNELING RADIATION FROM 100-800 MEV ELECTRONS AND POSITRONS IN THIN C, Si AND Ge CRYSTALS

The characteristics of radiation by relativistic electrons and positrons at (100) and (110) planar channeling in C, Si, Ge crystals (CR – channeling radiation) are studied theoretically in details in Ref. [2.1] using a separate crystallographic plane potential approximated by simple function

called the “inverse parabola”. However, at planar channeling in such crystals along so called double planes (111), the analytical solution to the problem is difficult and, in order to evaluate the spectral-angular distribution of CR one has to use numerical methods to define both the particle trajectory and Fourier components of the radiation field. To determine a trajectory, one can use either the binary collision model, e.g. described in Ref. [2.2], or realistic planar potential followed by the numerical solution of the equation of motion.

2.1 Equation of motion, trajectories and velocities of electrons in a (111) planar channel

For the (111) planar channeling the electron motion can be considered as free along the channeling planes, while the transverse motion (along the x direction perpendicular to the planes) is determined by periodic potential energy $U(x)$, which is shown in Fig.2.1. Indeed, the relativistic equation of motion reads

$$\frac{d\vec{p}}{dt} = \frac{d}{dt}\left(\frac{m\vec{\mathrm{v}}}{\sqrt{1-\mathrm{v}^2/c^2}}\right) = \vec{F} = -\frac{\partial U(x)}{\partial x}\cdot\vec{e}_x\,, \tag{2.1}$$

from which the conservation of longitudinal (parallel to a plane) component of a particle momentum is resulted. Taking it into account and assuming the incident particle energy to be much greater compared to the potential energy $U(x)$, with a good accuracy one obtains the equation of transverse motion

$$\gamma m\ddot{x} = F = -\frac{\partial U(x)}{\partial x}, \qquad \gamma = \frac{1}{\sqrt{1-\mathrm{v}_{\|}^{\,2}/c^2}}\,. \tag{2.2}$$

The initial conditions are: the point of incidence into a crystal $x(t=0)\equiv x_0$ and transverse momentum $\vec{p}_x(t=0) = \vec{p}\vartheta_0$ - which define the integral of motion (2.2), so-called “transverse energy”:

$$\varepsilon_\perp = U(x_0) + \frac{\vec{p}_\perp^{\,2}}{2\gamma m} = U(x_0) + \frac{\vec{p}^{\,2}\vartheta_0^2}{2\gamma m}\,. \tag{2.3}$$

The solution of Eq.(2.2) was performed numerically. In contrary to the (100) and (110) channeling considered in [2.1] when we have two types of the trajectories, under motion in the potential of double planes one obtains three types of the Eq.(2.2) solutions for both transverse coordinate and velocity, which describe the motion of channeled (under-barrier) or quasi-channeled (above-barrier) electrons.

$$\dot{x}_{cd}(t),\ -U_0 \le \varepsilon_\perp \le U_1,\ -\frac{T_{cd}}{2} \le t \le +\frac{T_{cd}}{2}\,. \tag{2.4a}$$

$$\dot{x}_{cu}(t),\ U_1 \le \varepsilon_\perp \le 0,\ -\frac{T_{cu}}{2} \le t \le +\frac{T_{cu}}{2}\,. \tag{2.4b}$$

$$\dot{x}_{nc}(t),\ 0 \le \varepsilon_\perp,\ -\frac{T_{nc}}{2} \le t \le +\frac{T_{nc}}{2}\,. \tag{2.4c}$$

Here, $\dot{x}_{cd}(t)$ is the velocity of electron bounded with one plane in (111) planar channel (negative transverse energy); $\dot{x}_{cu}(t)$ is the velocity of electron bounded with two planes in

(111) planar channel (negative transverse energy); $\dot{x}_{nc}(t)$ is the velocity of electron moving above barrier formed by periodic (111) planar potentials (positive transverse energy).

In accordance with the motion types, there appear three different groups of the motion periods: two groups for channeled electrons, T_{cd} and T_{cu}, and one for above-barrier electrons, T_{nc}.

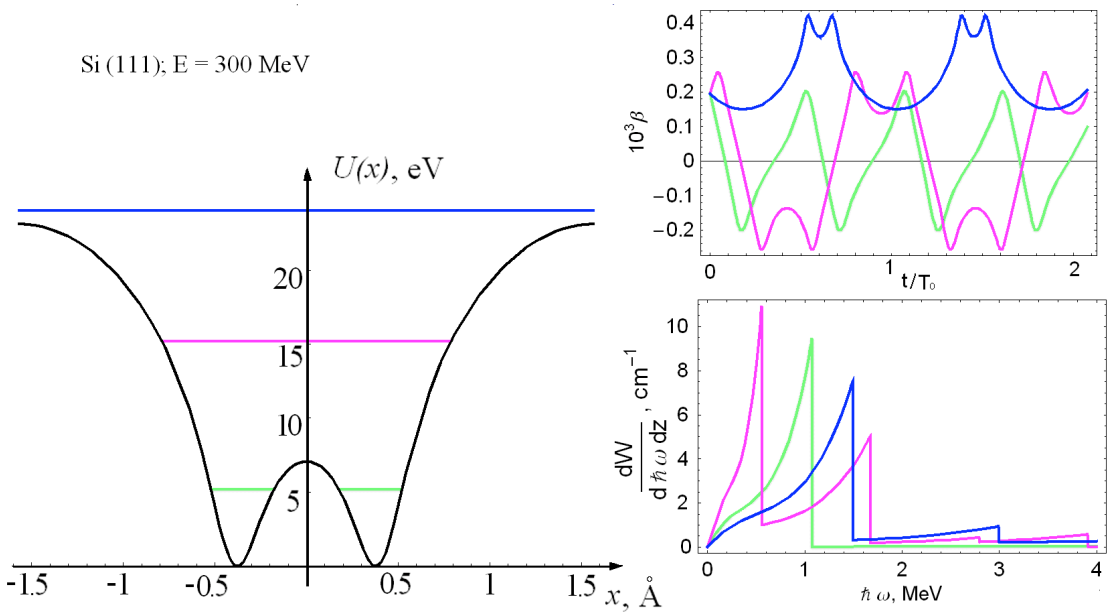

Figure 2.1. Left part: potential energy of electron in the system of double planes Si (111) and three values of transverse energy, corresponding to the three types of motion. Right part: time dependence of transverse velocity for three indicated values of transverse energy and radiation spectra for each of the trajectory. Here, $T_0 = d/c\sqrt{2\varepsilon_\perp/U_0}$.

Thus, going from bound under-barrier motion of type “d” to the bound under-barrier motion of type “u”, the period of motion increases more than 2 times, therefore the characteristic frequency of radiation from under-barrier electrons of type “d” is approximately 2 times less. Further, going from bound under-barrier motion of type “u” to above-barrier motion, the period of motion decreases approximately 2 times, therefore the characteristic frequency of radiation from above-barrier electrons is 2 times less, i.e. becomes the same as for radiation from electrons of type “u”.

If the angle of electron entrance into a crystal with respect to the planes $\vartheta_0 \neq 0$, electrons with $\varepsilon_\perp < 0$ are captured into a channel and moving in a bound state with one or two planes; electrons with $\varepsilon_\perp > U_0$ are moving out of one channel, crossing subsequently the periodically arranged crystal planes. The radiation from these three groups can not be separated in principle, since in a real experiment, electrons enter a crystal at different both points $x_0 \rightarrow U(x_0)$ and angles of incidence, therefore, receiving different values of the transverse energy.

2.2 Spectral characteristics of radiation from (111) and (100) planar channeled electrons in Si crystal – theory and model for calculations

If both the trajectory and velocity of planar-channeled electrons are defined, the characteristics of radiation from above-barrier and under-barrier electrons can be calculated within the frame of

classical electrodynamics valid, depending on the crystal type, for electron energies ranging from 100 MeV to a few GeV. The spectral-angular distribution of radiation intensity into a given direction $\vec{n}$ is determined by the formula (see, e.g. [2.1,2.3])

$$\frac{dW}{d\omega d\Omega} = \frac{e^2}{4\pi^2 c^3} \cdot \left| \int_{-\infty}^{+\infty} \frac{\left[\vec{n} \times \left[\left(\vec{n} - \vec{\beta}\right) \times \vec{w}\right]\right]}{\left(1 - \vec{n} \cdot \vec{\beta}\right)^2} \cdot \exp\left\{ i\left(\omega t - \vec{k} \cdot \vec{r}(t)\right)\right\} dt \right|^2 . \tag{2.5}$$

Here, $\vec{n}$ is the unit vector in the direction of emission, $\vec{\beta} = \vec{\mathrm{v}}/c$ and $\vec{w}$ are the particle velocity and acceleration, respectively, ω is the frequency of emitted photon, and $\vec{k} = \omega \vec{n}/c$ is the photon wave vector; the trajectory and velocity are defined by $\vec{r}(t) = \vec{e}_x \cdot x(t) + \vec{\mathrm{v}}_{\|} \cdot t$ and velocity $\vec{\mathrm{v}}(t) = \vec{e}_x \cdot \dot{x}(t) + \vec{\mathrm{v}}_{\|}$, correspondingly. At the given point and angle of incidence, the electron motion is quasi-periodic in transverse coordinate $x(t)$, with the period of motion $T = T(\varepsilon_{\perp})$, therefore Eq.(2.5) can be presented in the form

$$\frac{dW}{d\omega d\Omega} = \frac{e^2}{4\pi^2 c^3} \cdot \left(\frac{\omega}{\tilde{\omega}}\right)^4 \cdot \left| \left[\vec{n} \times \left[\left(\vec{n} - \vec{\beta}\right) \times \vec{w}_{\tilde{\omega}}\right]\right] \right|^2 . \tag{2.6}$$

$$\left|\vec{w}_{\tilde{\omega}}\right|^2 = \left|\vec{w}_{\tilde{\omega}}^{\,T}\right|^2 \cdot \left| \sum_{n=1}^{N} \exp\left(i(n-1)\tilde{\omega}T\right) \right|^2 = \left|\vec{w}_{\tilde{\omega}}^{\,T}\right|^2 \cdot \frac{\sin^2\left(N\tilde{\omega}T/2\right)}{\sin^2\left(\tilde{\omega}T/2\right)}$$

$$\tilde{\omega} = \omega\left(1 - \vec{n}\vec{\beta}\right) \cong \frac{\omega}{2}\left(\gamma^{-2} + \vartheta^2\right)$$

Here, N is the number of electron oscillations at passage through a crystal. Further, we integrate over emission angles taking into account that for relativistic particle $\vec{w} \cong \vec{w}_{\perp} \perp \vec{\mathrm{v}}_{\|}$ and the photons are emitted at small angles with respect to the mean particle velocity. Further integration of (2.6) over polar emission angle is performed using the "dipole" approximation (which is equivalent to the substitution $\vec{n} \cdot \vec{r}(t) \cong \vec{n} \cdot \vec{\mathrm{v}}_{\|} t$ in argument of the exponential) and we derive the expression

$$\frac{dW}{d\omega} = \frac{e^2 \omega}{2\pi c^3} \int_{\tilde{\omega}/2\gamma^2}^{\infty} \frac{d\tilde{\omega}}{\tilde{\omega}^2} \cdot \left| w_{\tilde{\omega}} \right|^2 \cdot \left[1 - \frac{\omega}{\gamma^2 \tilde{\omega}} + \frac{\omega^2}{2\gamma^4 \tilde{\omega}^2}\right]. \tag{2.7}$$

If, $N >> 1$, we make use of the approximation

$$\left.\frac{\sin^2\left(N\tilde{\omega}T/2\right)}{\sin^2\left(\tilde{\omega}T/2\right)}\right|_{N>>1} \rightarrow 2\pi N \cdot \sum_{n=-\infty}^{+\infty} \delta\left(\tilde{\omega} - 2\pi n/T\right),$$

Eq. (2.7) transforms then into the known formulae for the spectral distribution of CR [2.1,2.3]:

$$\frac{dW}{d\omega\, dz} = \frac{e^2 \omega}{c^4 T^2} \sum_{l=1}^{\infty} \Theta\left(1 - \eta_l\right)\left(1 - \eta_l + \frac{1}{2}\eta_l^{\,2}\right)\left|\dot{x}_{\tilde{\omega}}^{T}\right|^2, \tag{2.8}$$

$$\tilde{\omega} = \frac{2\pi\, n}{T} \ ,$$

where the quantity η_l for under-barrier and above-barrier motion equals to

$$\eta_l^c = \frac{T\omega}{2\pi\gamma^2(2l-1)}; \eta_l^{nc} = \frac{T\omega}{2\pi\gamma^2 l},\ l = 1,2,....$$

.

In our calculations, in contrary to [2.1,2.3], we define numerically both the period of motion and Fourier-component of velocity for every particle entering a crystal using the real planar potential $U(x)$

$$(\dot{x}_c)_{\tilde{\omega}} = \int_{-T_c/2}^{T_c/2} \dot{x}_c e^{i\tilde{\omega}t} dt, \qquad (\dot{x}_{nc})_{\tilde{\omega}} = \int_{-T_{nc}/2}^{T_{nc}/2} \dot{x}_{nc} e^{i\tilde{\omega}t} dt, \tag{2.9}$$

where $\tilde{\omega}T_c = 2\pi(2l-1)$, $\tilde{\omega}T_{nc} = 2\pi l$, $l = 1,2,3,...$. As underlined first in [2.1], the under-barrier electrons radiate at odd harmonics while the above-barrier electrons radiate at even harmonics.

2.3 Spectral characteristics of radiation from planar-channeled electrons in Si (111) and (100) crystals: Results of numerical calculations

The formula (2.8) describes the radiation spectrum of one electron moving along quasi-periodic trajectory in a crystal. For further calculations, we substitute the numerically defined transverse velocity $\dot{x}(t)$ into Eq.(2.9).

The examples of calculated electron trajectories of type “nc”, “u”, “d” (three different values of transverse energy $\varepsilon_\perp$) and corresponding radiation spectra are presented in Fig.2.1.

In order to compare our calculations with experimental data, all characteristics should be averaged over various points of incidence x_0 into the crystal. This averaging results in the spectral distribution of CR, which depends now on the angle of incidence ϑ_0 of electron beam with respect to crystallographic planes.

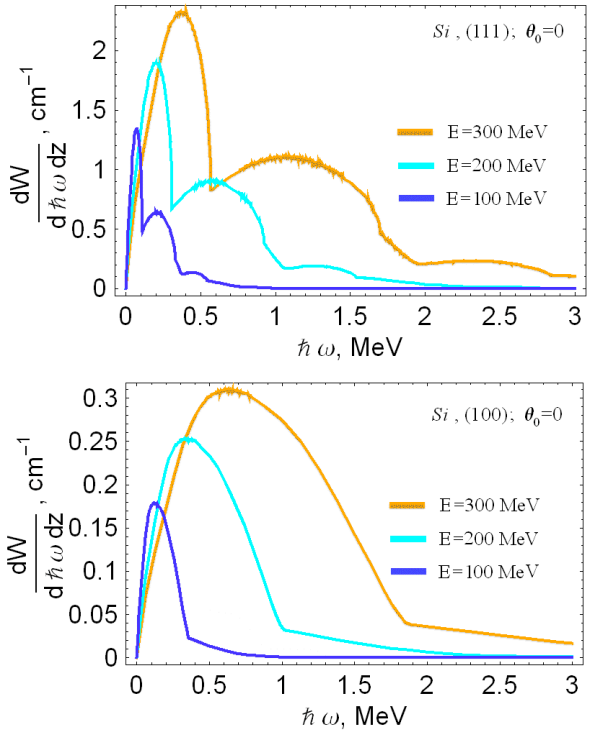

Figure 2.2. Energy dependence of radiation spectra from (111) and (100) channeled electrons for the angle of incidence $\vartheta_0 = 0$.

Let us first consider a special case, i.e. the angle of incidence of electrons with respect to the crystallographic planes (111) and (100) equals zero, $\vartheta_0 = 0$. The calculated spectra of CR are presented in Fig. 2.2 for three values of incident electron beam: 100, 200 and 300 MeV. Here, the absolute values of intensity are given, therefore one can see both the predicted by theory [2.2] shift of the maximums in the CR spectra and increase of the yield of CR. The breaks on the curves correspond to the maximum frequency of harmonics. Indeed, for (111) planes there are two groups of under-barrier electrons (two characteristic frequencies) and n=1,3 … harmonics contributes to the spectrum, while for (100) channeling there is only one group of under-barrier electrons which may radiate at n=1,3 … harmonics.

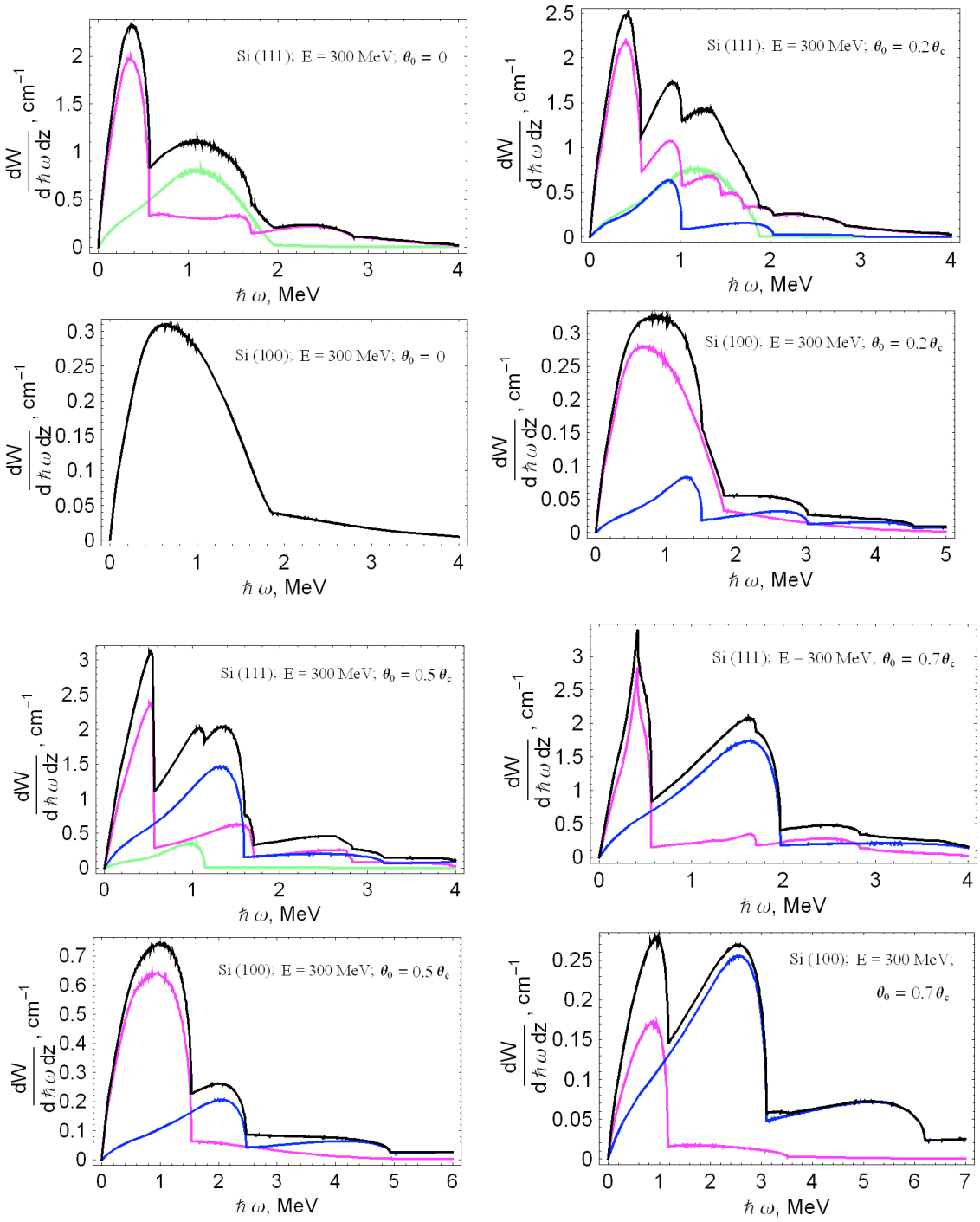

Figure 2.3. Evolution of CR spectra from 300 MeV electrons under the increase of the incidence angle with respect to the (111) and (100) planes of Si crystal (orientation dependence). The angles of incidence are: $\vartheta_0 = 0$, $\vartheta_0 = 0.2\vartheta_C$, $\vartheta_0 = 0.5\vartheta_C$, $\vartheta_0 = 0.7\vartheta_C$. Different colors denote: green – contribution from "d", pink – contribution from "u" and blue - contribution from "nc" electrons. The black curve is the total radiation spectrum, which is the sum of all contributions.

Fig. 2.3 shows the averaged over points of incidence of electrons into a crystal x_0 CR intensity spectrum (per unit path) for different angles of incidence with respect to the (111) and (100) planes of Si crystal. The absolute values of intensity are given, therefore one can see both the change of the shape of CR spectra and the yield of CR. In contrary to Fig. 2.2, there appears principal difference for (100) and (111) cases:

- In (100) case, it is seen clearly that the group of above-barrier electrons begins to play its role at $\vartheta_0 > 0$, which results in appearance of the new maximum in a more "hard" part of the radiation spectrum, since the characteristic period of motion of under-barrier electrons is almost twice as for above-barrier electrons. In addition, the characteristic breaks on the curves take place at the maximum frequencies of harmonics.
- In (111) case, it is seen clearly that the appearance of new maximums is due to redistribution of electrons over groups of type "u", "d" and "nc" following an increase of the angle of incidence. Additional characteristic breaks on the curves take place at the maximum frequencies of harmonics, which are different for electrons belonging to different groups.

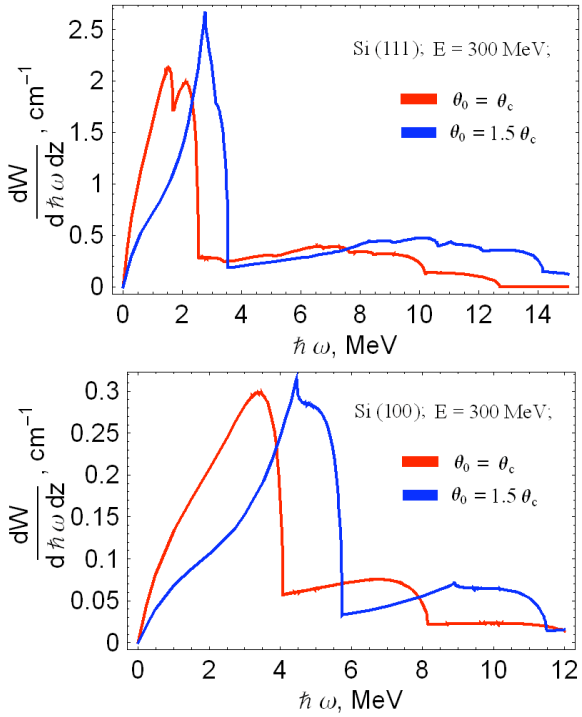

Figure 2.4. Radiation spectra from above-barrier 300 MeV electrons in (100) and (111) Si crystal for two angles of incidence: $\vartheta_0 = \vartheta_C$ (red curve) and $\vartheta_0 = 1.5\vartheta_C$ (blue curve).

Fig. 2.4 presents the averaged over x_0 radiation intensity spectra per unit path of electrons in a crystal, when the group of under-barrier electrons does not appear at all (strictly speaking, this result is valid only for a thin crystal, electron beam with zero angular divergence and when one neglects the capture into channeling regime due to various mechanisms). Here, the radiation spectra from above-barrier 300 MeV electrons in (100) and (111) Si crystal calculated for two angles of incidence $\vartheta_0 = \vartheta_C$ and $\vartheta_0 = 1.5\vartheta_C$ show the similar tendency , i.e. the shift of the

spectral maximum into a hard part of the spectrum. The difference of these spectra is obviously connected with different parameters of (100) and (111) planar periodic potentials.

For experimental studies at LNF electron/positron beams we are suggesting the following experiments on CR:

- Precision measurements of spectral-angular properties of CR from 100-800 MeV electrons and positrons in different thin crystals (studies on spectral distribution of radiation intensity using hard collimation of photon beam at different emission angles, at different angles of incidence) [2.4]
- Studies on spectral properties of linear polarization of planar channeling radiation from 100-800 MeV electrons and positrons (only a very few experiments have been performed up to now (see, e.g. [2.5-2.6] and references therein)
- Studies on transformation of channeling radiation spectra by increasing the electron/positron beam from 20 to 800 MeV: from line to continuous spectra, test of quantum versus classical description.
- Studies on the soft part of CR spectra from 100-800 MeV electrons and positrons (influence of medium permeability $\varepsilon(\omega)$)
- Applications: linear polirized gamma-source, slow positron production via CR, crystal orientation, crystal mosaicity, etc.

3. SPECIFIC ANGULAR DISTRIBUTION OF DIFFRACTED CHANNELING RADIATION: COMBINED EFFECT OF PARAMETRIC X-RADIATION AND CHANNELING RADIATION

The possible interplay of channeling radiation (CR) and parametric X-radiation (PXR) was discussed first in Ref. [3.1-3.3] using the kinematical theory of X-Ray diffraction. Later, more detailed theory have been developed using the dynamical theory of X-Ray diffraction and this effect was named DCR (Diffracted Channeling Radiation) [3.4]. The physics of the predicted effect is as follows: radiation, which virtually arises due to transition between transverse energy levels of channeled electron, is diffracted at another set of crystallographic planes and appears as radiation emitted at large (Bragg) angle with respect to the incident electron velocity. This effect was never observed before experimentally, and still exists as a challenge for experimentalists. Here, we analyze the new feature of this effect: orientation dependence of DCR angular distributions and propose possible experiments at LNF electron/positron beams.

3.1 Geometry of experiment to observe PXR and DCR

To observe the PXR and DCR at LNF one may use e.g. the same geometry as considered in [3.4], see in Fig. 3.1. Here, the electrons entering a crystal are captured into the channeling regime along (110) planes, while the DCR (diffracted channeling radiation) photons are emitted near the Bragg direction following the diffraction at $(1\bar{1}\bar{1})$ crystallographic planes.

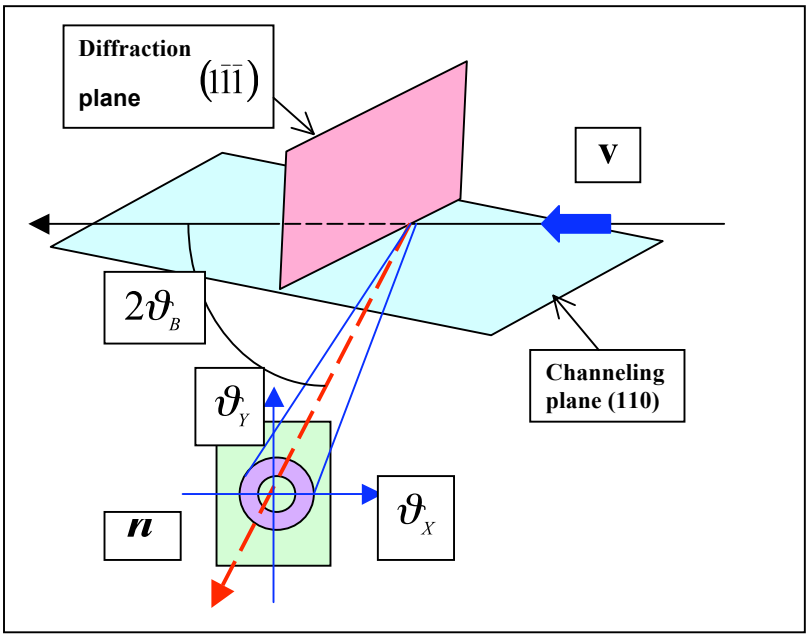

Figure 3.1. Arrangement of electron velocity $\mathbf{V}$, the (110) channeling plane and $(1\bar{1}\bar{1})$ diffraction plane in Si to observe the DCR. The direction of DCR photon emission (the Bragg direction) characterizes the unit vector $\boldsymbol{n}$. The Bragg angle ϑ_B and angular coordinates ϑ_X, ϑ_Y (two angles for calculation of DCR angular distribution in the plane perpendicular to $\boldsymbol{n}$) are shown, too.

3.2 Energy and momentum conservations for DCR in a crystal

If the DCR photon with energy $\hbar\omega$ is emitted, the energy conservation law reads

$$E_i - E_f = \hbar\omega \ , \tag{3.1}$$

where, the energies of the initial and final states of a channeling electron are:

$$E_i \approx E(\mathbf{p}_\parallel) + \varepsilon_i, \qquad E(\mathbf{p}_\parallel) = \sqrt{(c\mathbf{p}_\parallel)^2 + m^2c^4} \ ;$$
$$E_f \approx E(\mathbf{p}_\parallel') + \varepsilon_f, \quad E(\mathbf{p}_\parallel') = \sqrt{(c\mathbf{p}_\parallel')^2 + m^2c^4} \ .$$

Here, $\mathbf{p}_\parallel, \mathbf{p}_\parallel'$ are the longitudinal (along the channel) electron momentums before and after photon emission and $\varepsilon_i, \varepsilon_f$ are quantized transverse energies of electron in the (110) channel.

Since the transverse states of the channeled electron are bound, the momentum conservation works now only in direction parallel to the channeling planes. In a crystal, the momentum transferred should equal to one of the vectors $\mathbf{g}$ of a reciprocal lattice, therefore:

$$\mathbf{p}_\parallel - \mathbf{p}_\parallel' = \hbar(\mathbf{k}_\parallel + \mathbf{g}_\parallel), \tag{3.2}$$

where, $\mathbf{k}$ is the photon wave vector and $\mathbf{k}_\parallel$ is its projection onto channeling plane.

Combining (3.1) and (3.2), and assuming $\hbar\omega << \{ E_i, E_f \}$, one obtains the universal formula for the DCR photon frequency [3.4]

$$\omega = \omega_{DCR} = \frac{\mathbf{g}\cdot\mathbf{v}_\parallel + \Omega_{if}}{1 - \beta_\parallel^* \cos\Theta}, \tag{3.3}$$

where $\omega = c^* |\mathbf{k}|$, $\Omega_{if} = \left(\varepsilon_i - \varepsilon_f\right)/\hbar$, $c^* = c/\sqrt{\varepsilon_0}$, ε_0 is the average dielectric constant, $\beta_{\|}^* = \upsilon_{\|}/c^*$, $\upsilon_{\|}$ the velocity of the electron along the channel, and Θ observation angle.

The universal character of Eq.(3.3) becomes clear if one considers two limiting cases: if $\Omega_{if} = 0$, Eq.(3.3) reduces to the formula for parametric X-radiation (PXR)

$$\omega = \omega_{PXR} = \frac{\mathbf{g}\cdot\mathbf{v}_{\|}}{1-\beta_{\|}^*\cos\Theta}; \tag{3.4}$$

if $\mathbf{g} = 0$, Eq.(3.3) reduces to the formula for channeling radiation (CR)

$$\omega = \omega_{CR} = \frac{\Omega_{if}}{1-\beta_{\|}^*\cos\Theta}. \tag{3.5}$$

Let ω_B represent the frequency of photon satisfying the Bragg condition $\omega_B = c|\mathbf{g}|/2\sin\theta_B$, where θ_B the Bragg angle. If the condition

$$\omega_{CR} \cong \omega_B \tag{3.6}$$

is satisfied, the CR photon will be diffracted in a crystal.

3.3 Angular distribution of PXR

The angular distribution of PXR in the plane perpendicular to the Bragg direction (see Fig. 3.1) emitted per unit path of electron is described by the expression obtained using the dynamical theory of X-ray diffraction and plane wave functions of electrons (before and after emission) penetrating through a crystal [3.3]

$$\left(\frac{dN}{d\theta_x d\theta_y dz}\right)_{PXR} = \frac{\alpha\omega_B}{4\pi c\ \sin^2\theta_B}\left(\frac{\vartheta_x^2}{4\left(1+W_{\|}^2\right)} + \frac{\vartheta_y^2}{4\left(1+W_{\perp}^2\right)}\right) \tag{3.7}$$

$$W_\sigma = \frac{1}{2|\chi_g|P_\sigma}\left[\vartheta_x^2 + \vartheta_y^2 + \vartheta_{kin}^2 - \frac{|\chi_g|^2 P_\sigma^2}{\left(\vartheta_x^2 + \vartheta_y^2 + \vartheta_{kin}^2\right)}\right]$$

$$\sigma = \perp,\| \quad \rightarrow \quad P_\perp = 1, \qquad P_{\|} \cong \cos\left(2\vartheta_B\right)$$

$$\vartheta_{kin}^2 = \gamma^{-2} + \left|\chi_0(\omega_B)\right|, \qquad \chi_0(\omega) = -\frac{\omega_0^2}{\omega^2}\ ,\ \chi_g = -\frac{\omega_g^2}{\omega^2}$$

$$\omega_g^2 = \omega_0^2 \cdot \left[\frac{F(\boldsymbol{g})}{Z}\right] \cdot \left[\frac{S(\boldsymbol{g})}{N_0}\right] \cdot \exp\left(-\frac{\boldsymbol{g}^2\overline{u}^2}{2}\right),$$

Here:

α is the fine structure constant ;

ω_0 is the plasma frequency of a crystal ($\hbar\omega_0$ = 31 eV for Si)

$S(\boldsymbol{g})$ is the crystal structure factor of an elementary cell containing N_0 atoms ($N_0 = 8$ for silicon crystal);

$F(\boldsymbol{g})$ is the atomic form-factor;

Z is the number of electrons in an atom;

$\chi_0(\omega)$ and $\chi_g(\omega)$ are the coefficients in the Fourier series for the crystal dielectric permeability:

$$\varepsilon(\omega,\boldsymbol{r}) = 1 + \chi_0(\omega) + \sum_{\boldsymbol{g}\neq 0}\chi_{\boldsymbol{g}}(\omega)\cdot e^{i\boldsymbol{g}\cdot\boldsymbol{r}},$$

The Debye-Waller factor $\exp\left(-\boldsymbol{g}^2\overline{u}^2/2\right)$ takes into account the thermal vibrations of the crystal atoms, which decrease the coherent scattering, and, in addition, lead to the diffusion scattering of X-rays ($\overline{u}^2$ is the mean square amplitude of thermal vibrations of atoms). Specific angular distribution of PXR near the Bragg direction arises due to scattering of virtual photons by a crystal, since the virtual photons associated with electromagnetic field of relativistic particle moving in a medium are concentrated within a cone with angular width of the order of $\sqrt{\gamma^{-2} + |\chi_0(\omega_B)|}$.

3.4 Angular distribution of DCR

The angular distribution of DCR in the plane perpendicular to the Bragg direction (see, in Fig. 3.1) emitted per unit path of electron is described by the expression obtained using the dynamical theory of X-ray diffraction and specific wave functions of planar channeled electrons (plane wave penetrating along channeling planes and bound state with a plane in direction perpendicular to a channeling plane) [3.3]. This expression is valid for chosen $i \to f$ transition between transverse energy levels of channeled electron in a crystal:

$$\left(\frac{dN}{d\theta_x d\theta_y dz}\right)^{if}_{DCR} = \frac{\alpha\omega_B^3\cdot|y_{if}|^2}{4\pi c^3\sin^2\theta_B}\left(\frac{\vartheta_x^2\vartheta_y^2}{4\left(1+W_{\parallel}^2\right)} + \frac{\left(\vartheta_y^2 - \dfrac{\Omega_{if}}{\omega_B}\right)^2}{4\left(1+W_{\perp}^2\right)}\right) \tag{3.8}$$

$$\Omega_{i,f} = \left(E_{\perp,i} - E_{\perp,f}\right)/\hbar\ ,\ W_{\sigma} = \frac{1}{2|\chi_g|P_{\sigma}}\left[R - \frac{|\chi_g|^2 P_{\sigma}^2}{R}\right]$$

$$R = \left(\theta_x - \frac{\Omega_{if}}{\omega_B}\cot\theta_B\right)^2 \theta_y^2 + \gamma^{-2} + |\chi_0| - 2\frac{\Omega_{if}}{\omega_B},$$

Here, the dipole matrix element of $i \to f$ transition is defined as

$$y_{if} = \int_{-d/2}^{+d/2}\varphi^*{}_f(y)\cdot y\cdot\varphi_i(y)dy. \tag{3.9}$$

The integration is performed within periodicity interval $(-d/2,+d/2)$ assuming the appropriate normalization of both the initial $\varphi_i(y)$ and final $\varphi_f(y)$ channeled states.

The comparison of Eq.(3.8) with Eq.(3.7) shows new features in DCR angular distribution compared to that for PXR:

- One appears a very specific angular distribution of DCR due to scattering of virtual photon associated with $i \to f$ transition between two channeling states.
- The magnitude of these sharp peaks is defined by the dipole matrix element $|y_{if}|^2$. If one considers the isolated potential well, this matrix element equals zero between bound states of different parity and it obviously decreases also for $f - i > 1$.

3.5 Orientation dependence of DCR angular distribution

Since Eq.(3.8) refers only to fixed $i > f$ transition, to analyze a real problem one needs to take into account both the contributions from other transitions and population of initial channeled states. If the electron beam energy is fixed, population depends on the angle of incidence with respect to the channeling planes. Strictly speaking, population depends also on the penetration depth due to various inelastic processes (lifetime of channeled state), but in the case of a thin crystal (e.g. 50 μm for 100-800 MeV electrons) one can consider it as a constant value given by the angle of incidence. Thus, the formula for realistic numerical calculation of DCR (under-barrier transitions) reads

$$\left(\frac{dN}{d\theta_x d\theta_y dz}\right)_{DCR} = \sum_{i>f} \left|C_i(\vartheta_0)\right|^2 \cdot \frac{\alpha\omega_B^3 \cdot \left|y_{if}\right|^2}{4\pi c^3 \sin^2\theta_B} \left(\frac{\vartheta_x^2 \vartheta_y^2}{4\left(1+W_{\parallel}^2\right)} + \frac{\left(\vartheta_y^2 - \frac{\Omega_{if}}{\omega_B}\right)^2}{4\left(1+W_{\perp}^2\right)} \right) \quad (3.10)$$

Here, population of the i -th state $\left|C_i(\vartheta_0)\right|^2$ is defined as:

$$\left|C_i(\vartheta_0)\right|^2 = \frac{1}{d}\left|\int_{-d/2}^{+d/2} \exp\left(-ip\vartheta_0 \cdot y/\hbar\right) \cdot \varphi_i(y) dy\right|^2 . \quad (3.11)$$

where $p = \gamma\beta mc$ is the initial (before a crystal) momentum of electron and ϑ_0 the angle of incidence with respect to the channeling planes.

In order to calculate the total yield of X-ray photons near the Bragg direction, one should add PXRC (transitions with $i = f$, or intraband transitions), the angular distribution of which almost coincides with ordinary PXR, especially for above-barrier states with positive transverse energy [3.3]. Thus, in a good approximation we may write

$$\left(\frac{dN}{d\theta_x d\theta_y dz}\right)_{Bragg} = \sum_i \left|C_i(\vartheta_0)\right|^2 \left(\frac{dN}{d\theta_x d\theta_y dz}\right)_{PXRC}^{i} + \sum_{i>f} \left|C_i(\vartheta_0)\right|^2 \cdot \left(\frac{dN}{d\theta_x d\theta_y dz}\right)_{DCR}^{if} \cong ,$$

$$\cong \left[1 - \sum_i \left|C_i(\vartheta_0)\right|^2\right] \cdot \left(\frac{dN}{d\theta_x d\theta_y dz}\right)_{PXR} + \sum_{i>f} \left|C_i(\vartheta_0)\right|^2 \cdot \left(\frac{dN}{d\theta_x d\theta_y dz}\right)_{DCR}^{if} \quad (3.12)$$

where the summation is performed only over bound channeled states.

According to Eq. (3.12), in a thin crystal DCR is characterized by strong dependence on the angle of incidence ϑ_0 with respect to the channeling planes (orientation dependence) and on the initial energy of electrons (on relativistic factor γ), which defines the number of bound states with the channeling planes and transition frequency $\Omega_{i,f} = \left(E_{\perp,i} - E_{\perp,f}\right)/\hbar$ between them.

3.6 Numerical calculations of orientation dependence for angular distribution of DCR+PXRC

To use Eqs.(3.10-12), both $\varphi_i(y)$, $\varepsilon_i, \varepsilon_f$, $\left|y_{if}\right|^2$ and $\left|C_i(\vartheta_0)\right|^2$ have been obtained by many-beam calculations for (110) channeling, see in Fig. 3.2a-c. The representative calculations are performed for $\gamma = 100$ electrons channeled in (110) Si crystal. The results for band structure of

electronic energy levels and corresponding wave functions are shown in Fig. 3.2a and Fig. 3.2b, respectively. Fig. 3.2c shows the population $|C_i(\vartheta_0)|^2$ of under-barrier bands in dependence on the angle of incidence, while Fig. 3.2d presents the population of large number of both under-barrier and above-barrier bands but for the angle of incidence $\vartheta_0 = 0$. The transitions between different states in Fig. 3.2b may result in emission of X-ray photons, which due to diffraction are emitted at Bragg direction (see, in Fig. 3.1).

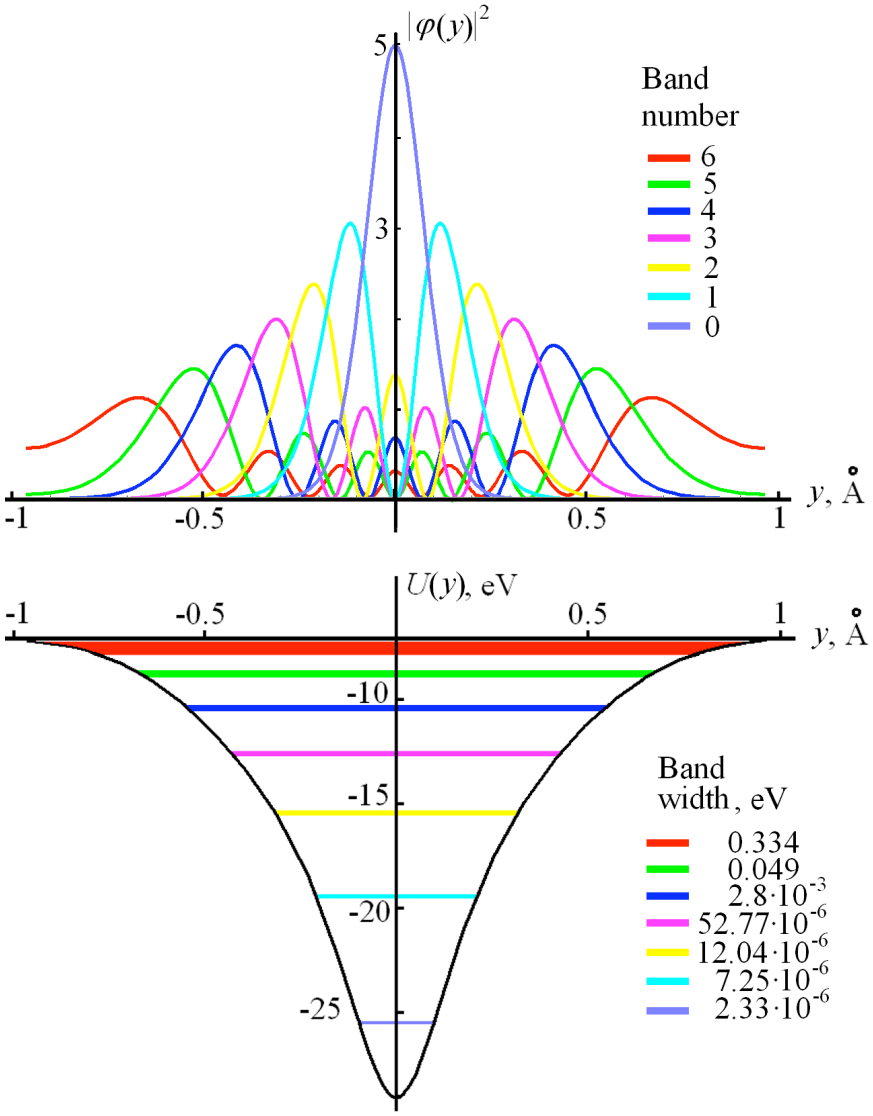

Figure 3.2. a) Band structure of transverse energy spectrum under (110) electron channeling in Si at $\gamma = 100$ (lower part); b) corresponding electron wave functions (upper part).

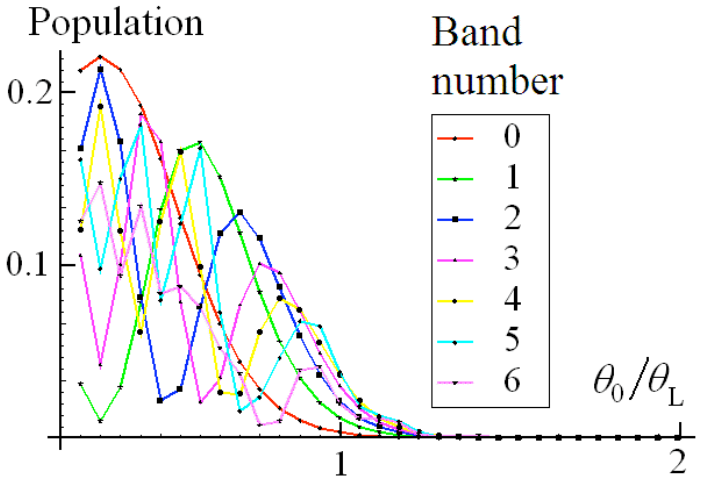

Figure 3.2 c. The population of sub-barrier energy bands shown in Fig. 3.2a, as a function of the angle of incidence ϑ_0 of electron beam with respect to the (110) channeling planes. Here, $\vartheta_L = \sqrt{2U/E}$ is the Lindhard critical angle.

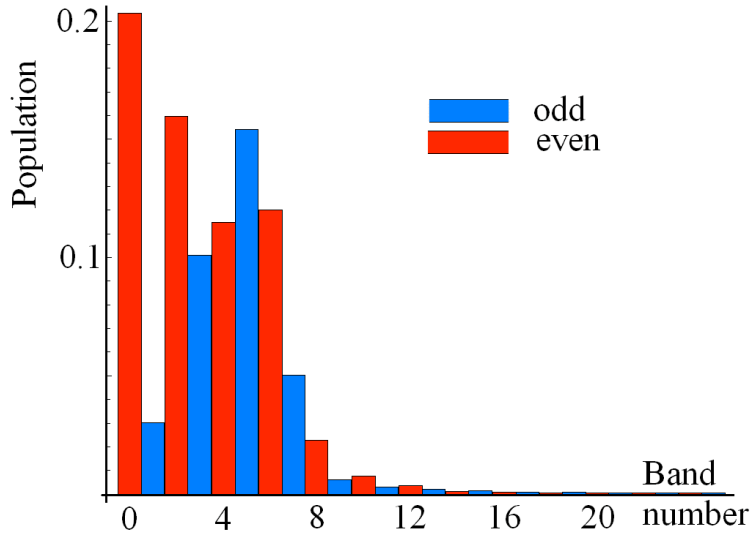

Figure 3.2d. The population of both under-barrier and above-barrier transverse energy bands for the angle of incidence $\vartheta_0 = 0$.

The results of calculations of DCR+PXRC angular distributions in the vicinity of the Bragg direction are shown in Fig. 3.3 for several values of the angle of incidence: $\vartheta_0 = 0; \vartheta_L/3; 2\vartheta_L/3; \vartheta_L$. Here, the parameters are: $\vartheta_B = \pi/8$, $(1\bar{1}\bar{1})$ diffraction planes, the DCR+PXRC photon energy equals $\hbar\omega_B = 8.441$ keV, the electrons are channeled along (110) planes in a Si crystal at $\gamma = 100$.

In calculations, we took into account all allowed transitions between transverse energy bands (in Fig. 3.2). The calculations show new features of DCR+PXRC:

- At fixed angle of incidence $\vartheta_0 \le \vartheta_L$, the angular distribution of DCR+PXRC as a function of two angular variables ϑ_X and ϑ_Y looks very specific. When cut along $\vartheta_X = 0$ or $\vartheta_Y = 0$ axes, it contains several sharp peaks in contrary to the angular distribution of ordinary PXR. The number of these peaks corresponds to the number of allowed dipole transitions between energy bands in Fig. 3.2b. If one assumes equal population of transverse energy bands This result coincides with given in Ref.[3.4]. In Ref.[3.5-3.6], similar results are obtained for (111) planar channeling of electrons in Si and LiF crystals.
- The shape of distribution changes with increase of the angle of incidence ϑ_0 confirming the change in population of transverse energy bands. As expected, at the angle of incidence $\vartheta_0 \ge \vartheta_L$ the specific fine structure of angular distribution of DCR+PXRC disappears and we obtain ordinary angular distribution of PXR.

In agreement with Ref. [3.4], the calculated peaks in DCR+PXRC are situated at emission angles smaller than that for ordinary PXR, i.e. at $\vartheta_{DCR} < \vartheta_{kin} = \gamma^{-2} + |\chi_0|$. In other words, DCR, similar to PXR, is concentrated around the Bragg direction but at the angles ϑ_{DCR} less than the characteristic angle ϑ_{kin} for PXR. Moreover, every sharp peak in Fig. 3 is splitted by

$$\Delta\vartheta_{DCR} \approx \sqrt{\chi_g} < \vartheta_{kin} = \sqrt{\gamma^{-2} + |\chi_0|}, \tag{3.13}$$

In order to show this, in Fig. A1 (Appendix 1) the 3D angular distribution of DCR+PXRC is shown in details for the case $\vartheta_0 = 0$.

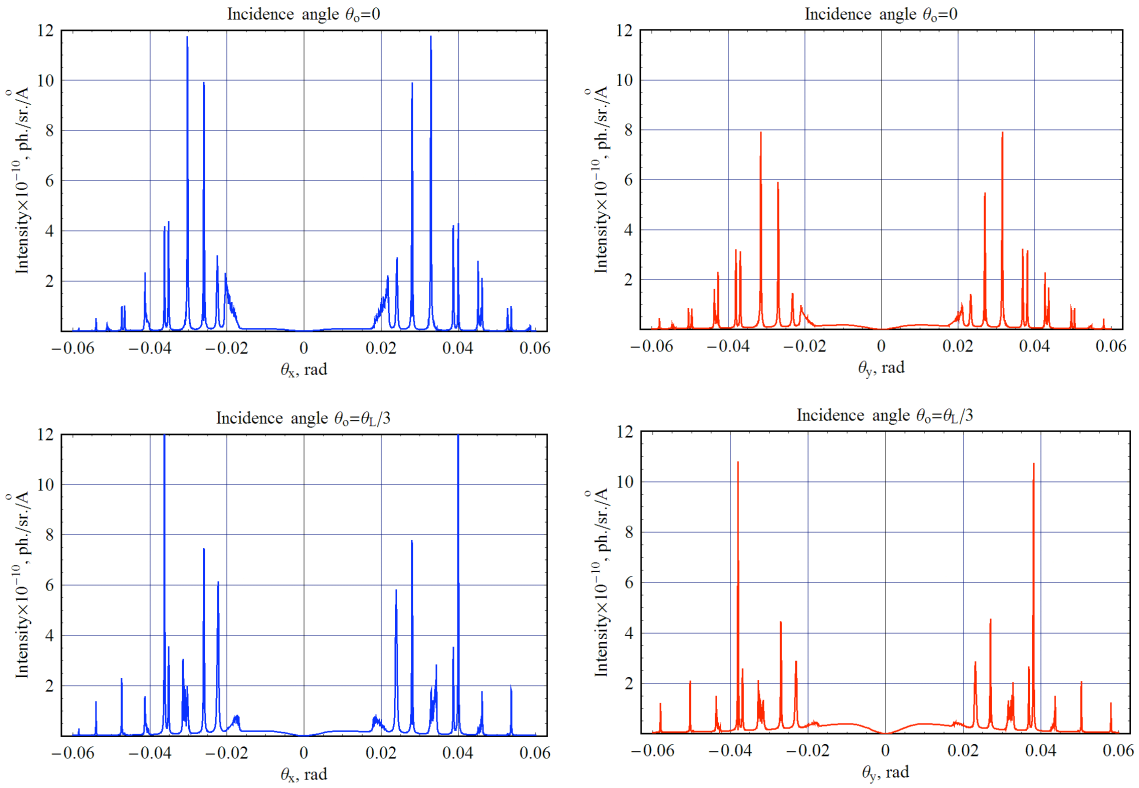

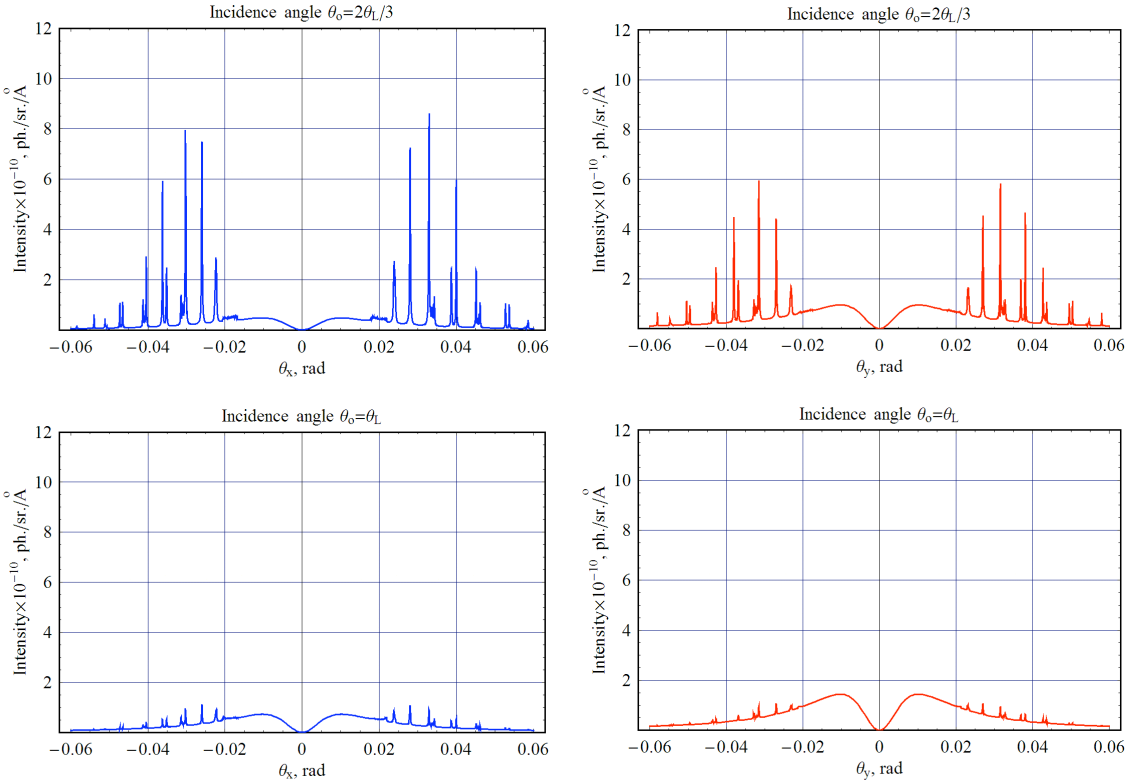

Figure 3.3. Angular distributions of DCR+PXR in vicinity of the Bragg direction: for $\vartheta_0 = 0, \vartheta_0 = \vartheta_L/3$, $\vartheta_0 = 2\vartheta_L/3$ and $\vartheta_0 = \vartheta_L$. Here, $\vartheta_X = \vartheta_Y = 0$ corresponds to the emission at the Bragg angle. Every ring-shaped distribution (in ϑ_X, ϑ_Y plane, see in Fig. A1) is cut here along ϑ_X axis at $\vartheta_Y = 0$ (left part) and along ϑ_Y axis at $\vartheta_X = 0$ (right part).

Thus, the specific orientation dependence of DCR+PXRC angular distribution in a thin crystal at the fixed electron beam energy may help in studies of this new effect. Of course, the life-time of transverse energy bands should be of the order of passage time through a crystal that means, for $\gamma = 100$ the crystal thickness should be of order of 20 μm.

To conclude, at LNF we may suggest new perspective experiments on:

- First observation and systematic studies of angular, spectral and polarization properties of DCR+PXRC from relativistic electrons, including electron beam energy dependence and orientation dependence
- First observation and systematic studies of PXR and DCR+PXRC from relativistic positrons.

These effects have been never observed before experimentally, and still exist as a challenge for experimentalists.

APPENDIX A: 2D angular distribution of DCR+PXRC

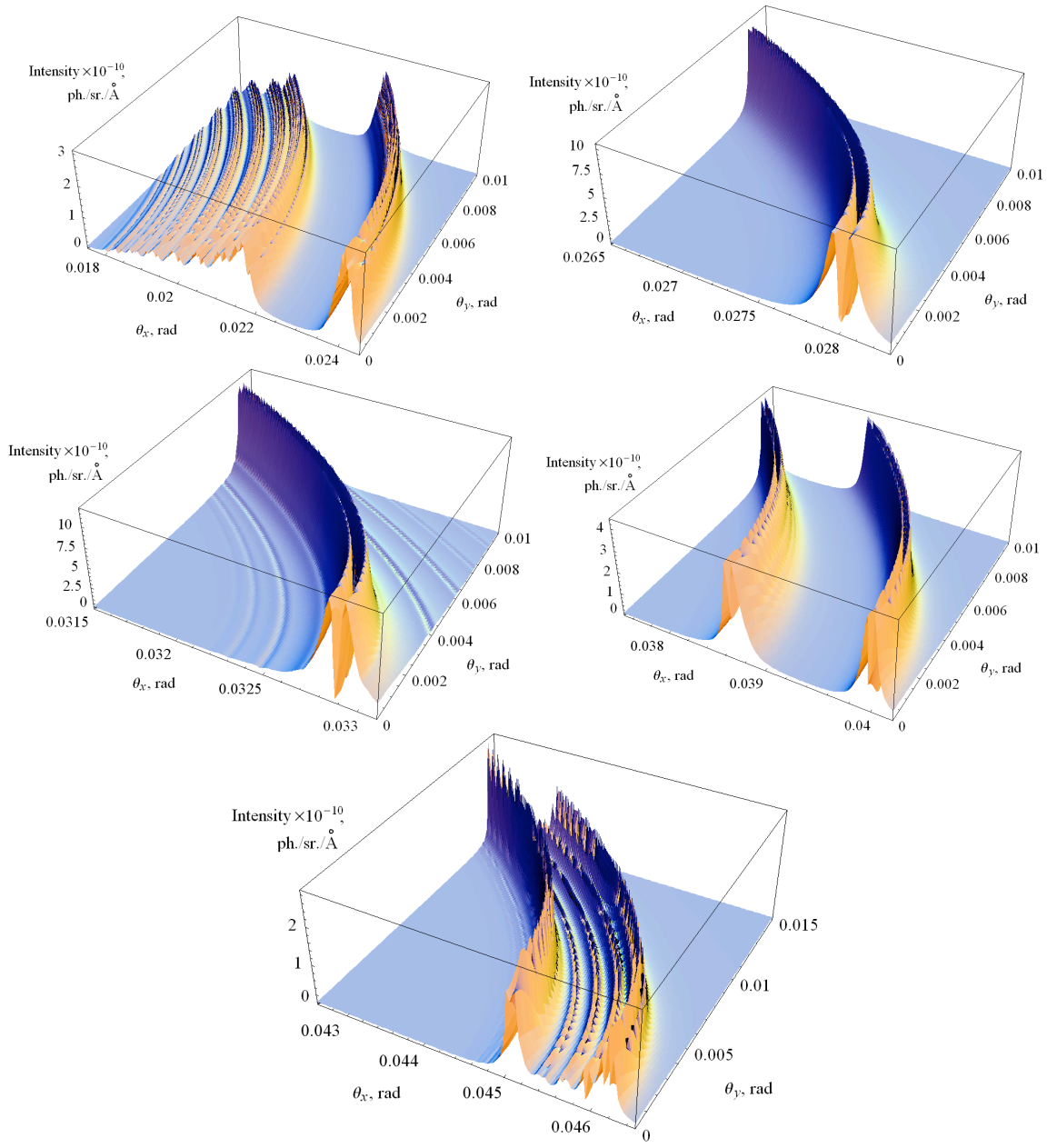

Figure 1A. Angular distribution of DCR from $\gamma = 100$ electrons under planar channeling in (110) Si crystal as the function of the angles ϑ_X and ϑ_Y in vicinity of the Bragg direction ($\vartheta_X = \vartheta_Y = 0$ correspond to the emission at the Bragg angle). The Bragg angle $\vartheta_B = \pi/8$, $(1\bar{1}\bar{1})$ diffraction planes, the DCR photon energy $\hbar\omega_{CR} = \hbar\omega_B = 8.441$ keV. In calculations, we took into account all allowed dipole transitions between transverse energy bands. The well pronounced rings correspond to the allowed dipole transitions, see in Fig. 3.2. Roughly speaking, the rings are placed above ordinary PXR angular distribution given by Eq.(3.7). Here, the angle of incidence $\vartheta_0 = 0$.

4. ENHANCED MULTIPLE SCATTERING OF 100 - 800 MEV ELECTRONS AND POSITRONS IN A THIN CRYSTAL

As shown in Ref. [4.1], multiple scattering of relativistic particles in a thin crystal may differ significantly from that in an amorphous target of the same thickness. Using the model of multiple scattering of particles on continuous potentials of atomic axes, the authors of [4.1] predicted the orientation dependence of the mean square muliple scattering angle and its significant enhancement at the angles of incidence of order of the Lindhard critical angle. Since this model takes into account only coherent scattering, i.e. does not take into account the thermal vibrations of the crystal atoms, the question on how incoherent scattering will change these results remains open. Here, in order to clarify this situation, we used more realistic model, i.e. binary collision model, and carried out computer simulations to study the orientation dependence of multiple scattering of relativistic electrons and positrons in a tungsten crystal. It should be noted, that at the moment the direct experimental verification of this effect vanishes.

4.1 Binary collision model

For the tracing of trajectories of electrons and positrons in a tungsten (W) crystal, a binary collision model (BCM) was used [4.2]. The process of relativistic particle scattering by a separate atom is described within the frame of classical (relativistic) mechanics. In BCM, the trajectory of the charged particle in a crystal is determined by a series of sequential independent collisions with atoms of crystal lattice. During simulation of particle trajectory the asymptotic approximation was used, i.e. the particle trajectory is represented by a curve, which is the sum of trajectory asymptotes in all-individual collisions. For determination of scattering angle in a separate collision, the formula for scattering angle on the Thomas-Fermi screened potential in Moliere's approximation was utilized.

Incoherent scattering, i.e. the influence of crystal temperature is taken into account through independent thermal vibrations of lattice atoms near their equilibrium positions. That means, each subsequent impact parameter of collision is selected taking into account the displacement of next atom from its equilibrium position in a lattice, with amplitude of deflection determined according the normal distribution law. For other details of the model see in [4.3-4.4].

4.2 Angular distributions of electrons and positrons passed through thin W crystal

The computer simulations showed that the type of electron or positron trajectory depends strongly on the point of incidence into a crystal. Schematically, one may say on areas of particles entry into a crystal as near the crystallographic axes and between crystallographic axes (Fig. 4.1).

Several typical trajectories of 500 MeV electrons and positrons in <100> W crystal, simulated for different points of particles incidence into a crystal, are presented in Figs. 4.2-5.

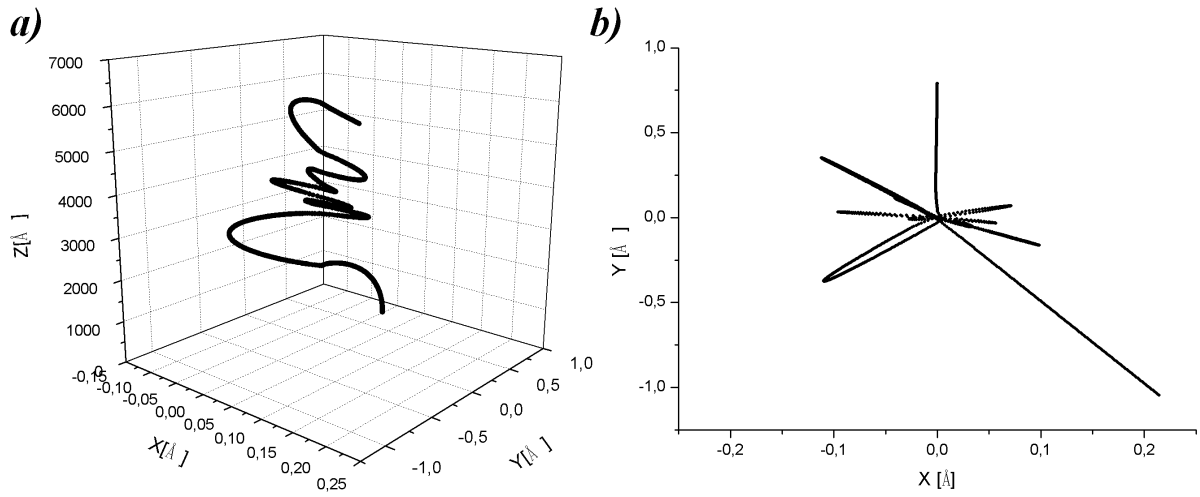

Figure 4.1. One of selected trajectories of 500 MeV electron in <100> W crystal (a) and its projection onto XY plane (b). Initial points of the entry (near axis): x_0=0 Å , y_0=0.79 Å z_0=0.0 Å . The crystal thickness along Z direction: $l \cong 0.631\,\mu m$ ($2*10^3$ collisions).

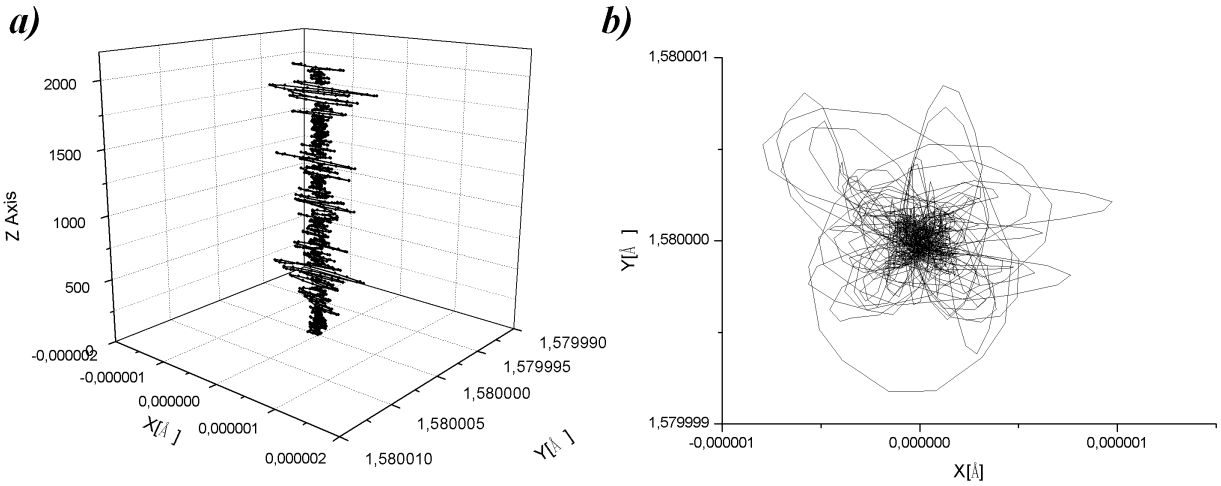

Figure 4.2. One of selected trajectories of 500 MeV positron in <100> W crystal (a) and its projection onto XY plane (b). Initial points of the entry (near axis): x_0=0 Å , y_0=1.58 Å , z_0=0.0 Å . The crystal thickness along Z direction : $l \cong 0.2\,\mu m$.

As follows from these Figs., the trajectories of positively and negatively charged particles, despite of the identical points of entry into a crystal target, differ sharply:

- electron, entering a crystal near to an <100> axis, moves further in a condition corresponding to classical axial channeling (see, in Fig. 4.2), in contrary to a positron, which during scattering on a single atomic string receives an angle (and transverse momentum) sufficient to leave a zone of interaction with this axis and to move to another nearest axis (see, in Fig. 4.3), i.e. a positron moves in a condition corresponding to classical quasi-channeling (or above-barrier motion);

• electron, entering a crystal between <100> atomic axes, moves in a condition corresponding to classical axial quasi-channeling (see, in Fig. 4.1), in contrary to a positron moving in a condition corresponding to classical hyper-channeling (see, in Fig. 4.2). For an electron, which is attracted by the axes, a probability to receive even small scattering angle, sufficient for the going out from a zone of interaction with atoms of these axes is large, in contrary to a positron, which is repulsed by the axes and moves between atomic strings.

The angular distributions of electrons and positrons penetrated through W crystal along <100> and <110> directions have been obtained in further set of computer experiments. The parameters of the computer experiments: $N = 10^4$ - is the number of particles in a computer experiment; $l \cong 31.6$ μm - *the* thickness of the crystal target; $\theta_{x0}, \theta_{y0} = 0$ - initial angles of entry of particles with respect to <100> and <110> crystallographic axes; $T = 293K$ - temperature of crystal (defines the thermal vibration amplitude, in our case $\sqrt{\overline{u^2}} = 0.053$Å); $E = 500$ MeV- energy of particles.

The results of computer simulations of angular distributions of electrons and positrons penetrated through W crystal are presented in Fig. 4.6-9. To summarize, the results of simulation are as follows:

• The shape and dimension of obtained angular distributions of electrons for <100> (Fig. 4.6) and <110> (Fig. 4.7) directions are practically the same and are characterized by well pronounced maximum at zero exit angles. The electron beam is dispersed practically in an identical range of exit angles: $-0.01 < \theta < 0.01$ rad.

• The shape and dimension of obtained angular distributions of positrons for <100> (Fig. 4.7) and <110> (Fig. 4.8) directions differ from that for electrons and are characterized by well pronounced minima at zero exit angles. The positron beam is dispersed practically in an identical range of exit angles: $-0.001 < \theta < 0.001$ rad, which is 10 times less than in the case of electrons.

Thus, the difference in the angular distributions of relativistic electrons and positrons passing through a thin crystal are quite large and should manifest itself e.g. in radiation spectra, in PXR angular distributions, etc. The analysis of the influence of multiple scattering on radiation spectra and photon angular distributions is in process and will be published separately.

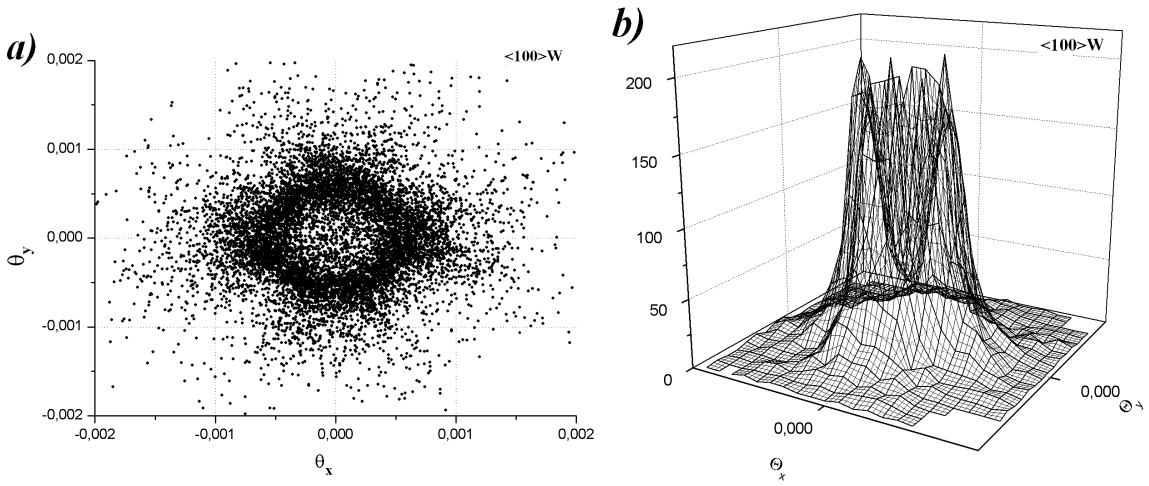

Figure 4.3. Angular distribution (a) and density of angular distribution (b) of positron

beam penetrated through the <100> W crystal with thickness $l \cong 31.6\,\mu m$, θ_x, θ_y - scattering angles (X-, Y-projection), $\theta_x = p_x/p_0, \theta_x = p_y/p_0$, p_0 – is initial momentum, while p_x and p_y are the momentum components in X and Y directions (transverse $< 100 >$ axis) after crystal.

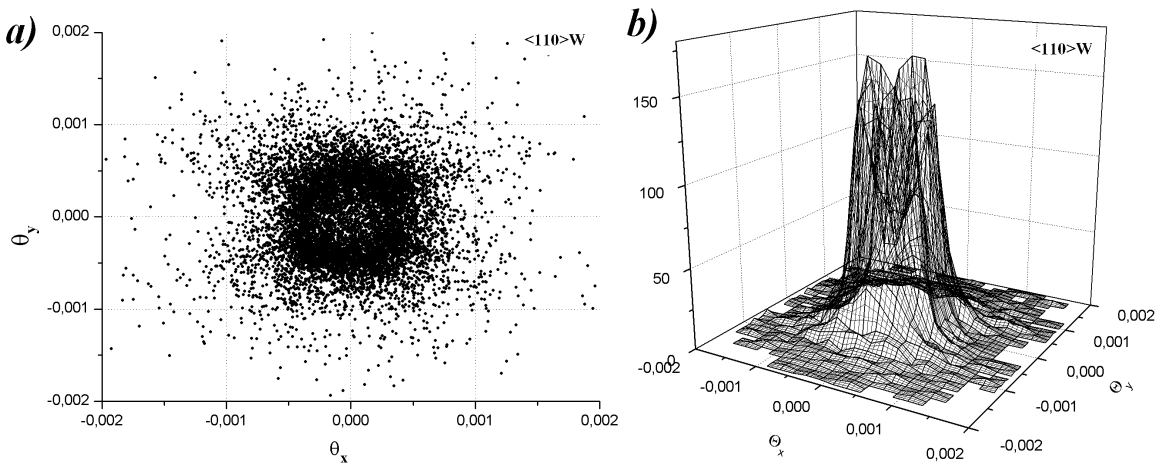

Figure 4.4. Angular distribution (a) and density of angular distribution (b) of positron beam penetrated through the <110> W crystal with thickness $l \cong 31.6\,\mu m$, θ_x, θ_y - scattering angles (X-, Y-projection), $\theta_x = p_x/p_0, \theta_x = p_y/p_0$, p_0 – is initial momentum, while p_x and p_y are the momentum components in X and Y directions (transverse $< 100 >$ axis) after crystal.

4.3 Mean square angle of multiple scattering of 500 MeV electrons and positrons in the tungsten crystal

As well known, the difference in scattering of relativistic electrons and positrons on a separate atom arises only in the quantum mechanics, in the second Born approximation (see, e.g. [4.1]). In the classical theory, the mean square angle of multiple scattering $\overline{\theta}^2$ is the same both for electrons and positrons.

The standard deflection of projection of multiple scattering angle of relativistic particles penetrated through amorphous target of the thickness x is given by the well known formula (see, e.g. [4.5]):

$$\theta_{ms} = \sqrt{\left\langle \overline{\theta}^2 \right\rangle} = \frac{13.6 MeV}{\beta c p} Z \sqrt{\frac{x}{X_0}} \left[1 + 0.038 \ln\left(\frac{x}{X_0} \right) \right]. \qquad (4.2)$$

In Eq. (4.2) , $\beta c = v$ is a particle velocity, p is its momentum, $Z = 1$ for our case of electrons and positrons and $X_0 = 0.35 cm$ is the radiation length of tungsten W.

The Table 1 presents the mean square values of projected multiple scattering angle, calculated using obtained in Sec.2 angular distributions for the W crystal target of the thickness $l \cong 3.16\ \mu m$ and two directions, and the value θ_{ms} in amorphous W target of the same thickness calculated according Eq.(4.2).

As it follows from the Table 1, even at zero angles of incidence there appears significant difference in the values of mean square multiple scattering angle for electrons and positrons. Comparing with amorphous target, we may comment, the angular distribution of 500 MeV electrons after penetration through a crystal is several times greater while that for positrons is approximately two times smaller.

The next peculiarity is that for a crystal the particles trajectories, the angular distribution and the mean square of multiple scattering angle depend on the angle of incidence φ with respect to the crystallographic axes. To study this dependence, the next set of computer experiments was carried out. The dependence of the ratio $\sqrt{\bar{\theta}^2/\bar{\theta}^2_{MS}}$ upon the angle of incidence φ is shown in Fig. 4.5 ($\bar{\theta}^2$ - is a mean square angle of multiple scattering in the <100> W crystal of the thickness $l \cong 31.6\,\mu m$ and $\bar{\theta}^2_{ms}$ is a mean square angle of multiple scattering in an amorphous target of the same thickness). In Fig. 4.10, the angle of incidence φ is measured in the values of the Lindhard angle φ_L:

$$\varphi_L = \sqrt{2eU_0/E} \quad , \tag{4.3}$$

where U_0 is the maximal value of continuous potential of the crystal axis (see, for example [4.1]).

The curve 3 in Fig. 4.5 shows also the results of the orientation dependence $\sqrt{\bar{\theta}^2/\bar{\theta}^2_{MS}} = R/4a_1\varphi$ calculated according formulas of the Ref. [4.1], in which the model of a multiple scattering of particles by continuous potentials of crystal axes was used.

From the obtained results it follows, that in the case of the aligned crystal target $\bar{\theta}^2$ depends on the sign of the particle charge and at small angles of incidence φ (the angle of incidence with respect both to a crystal axes and plane) significantly differs from $\bar{\theta}^2_{ms}$ in amorphous target of the same thickness. With increase of the angle of incidence into a crystal φ , the values of mean square scattering angle of electrons and positrons in a crystal approach to the values of the mean square angle of multiple scattering in an amorphous target. The difference in the scattering of particles with different sign of electric charge is determined by the difference in small-angle scattering of these particles on a separate string of atoms (crystal axis).

Our results obtained using BCM agree qualitatively with the data obtained on the basis of the model of particles scattering on a system of continuous potentials of the crystal axes, suggested in [4.1]. The advantage of the BCM model is that: a) the results of computer simulation do not depend on a choice of the form of continuous potential of an atomic string, as in [4.1], and b) it takes into account incoherent scattering, i.e. the thermal vibrations of the crystal atoms.

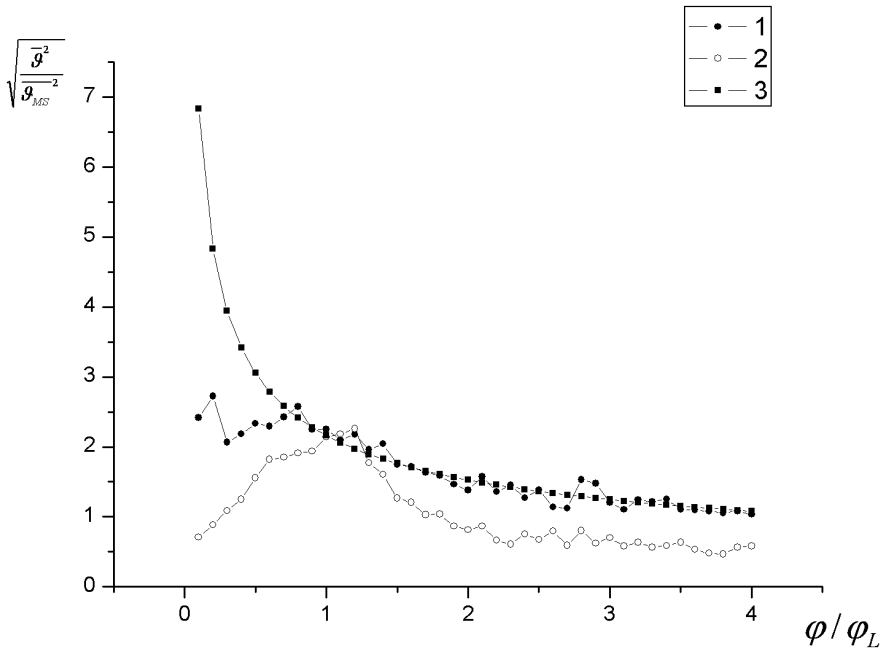

Figure 4.5. Orientation dependence of the mean square multiple scattering angle of 500 MeV electrons (curve 1) and positrons (curve 2) in $l \cong 31.6\,\mu m$ <100> W crystal. The curve 3 is calculated according theory [4.1], $\sqrt{\bar{\theta}^2/\bar{\theta}_{MS}^2} = R/4a_1\varphi$, where R is the distance between the atoms in the axis, a_1 is screening radius, φ is the angle of incidence into the crystal with respect to the crystallographic axis; φ_L is the Lindhard angle.

The computer experiments performed on the base of BCM clearly demonstrated significant difference in angular and spatial distributions of 500 MeV electrons penetrated through W crystal at identical initial conditions. At the same time, the mean square multiple scattering angle for positrons and electrons depends on the angle of incidence with respect to the crystallographic axes, and is greater in the case of electrons, especially at angles of incidence less than the Lindhard critical angle. In the case of electrons, the mean square multiple scattering angle exceeds the same value in an amorphous target of the same thickness, especially at the angles of incidence close to the Lindhard critical angle, see in Fig. 4.10. Our results obtained for relativistic electrons and positrons using BCM, agree qualitatively (at the angles of incidence greater than the Lindhard angle) with the theoretical estimations [4.1] based on the model of multiple scattering by continuous potentials of the crystal axes. Since our model takes into account the incoherent scattering not incorporated into model [4.1], i.e. thermal vibrations of the crystal atoms, the enhancement of the mean square multiple scattering angle at the angles of incidence close to the Lindhard critical angle over the same quantity in an amorphous target of the same thickness is less than in [4.1].

The computer experiments performed for electrons and positrons energies 100 MeV and 300 MeV in a tungsten and other crystals (C, Si, Ge, LiF), at different temperatures and alignments (including planar channeling case), demonstrate similar peculiarities of the multiple scattering. The computer experiments to study the influence of enhanced multiple scattering in a thin aligned crystal on electromagnetic radiation spectra, angular distributions and radiation loss are in progress and the results will be published elswhere. The possible application (for discussions)

of the difference in multiple scattering of negatively and positively charged particles in a thin aligned crystal could be the spatial separation of mixed beams of particles with different sign of electric charge.

Computer experiments to study spatial and angular distributions of relativistic electrons and positrons in a tungsten crystal are performed using the binary collision model. The results of computer experiments for <100> and <110> directions in a tungsten crystal showed that the mean square angle of multiple scattering depends on the particle charge sign and exceeds considerably the value of mean square multiple scattering angle in an amorphous target of the same thickness, in accordance with earlier theoretical predictions based on the model of multiple scattering by continuous potentials of the crystal axes.

Proposal for experimental studies at LNF:

1. First direct observation of predicted effect of enhanced multiple scattering of relativistic 100-800 MeV electrons and positrons in thin aligned crystals (detection of deflected particles)

2. Influence of enhanced multiple scattering on electromagnetic radiation spectra, angular distributions and yield of radiation.

5. ON POSSIBILITY OF SPIN MANIFESTATION IN CHANNELING RADIATION

As known the motion of spin particles is described by the Dirac equation [5.1]. Generally, due to negligible small spin-related terms in the Dirac equation, solving the motion equation for specified particles channeled in crystals, does not need to take into account the spin influence to "projectile-crystal" interaction and can be reduced to the Klein-Gordon equation [5.2].

Here we consider the planar channeling, when the particles move at small angle to the crystal plane. It is well known that transverse-plane motion of a channeled particle is characterized by a set of bound energy levels; the radiation spectrum is defined by the transitions between various levels. Solving the Dirac equation without simplifications at the beginning enables to obtain the bound energy levels in presence of a particle's spin. The similar application of Dirac equation to consider the axial channeling case was offered in [5.3].

In [5.4] the Dirac equation for ultra relativistic particles, which move in one-dimensional electric field under small angle to a plane orthogonal to the field, is solved. It is shown that one needs to solve the motion equations for two possible projections of a particle's spin onto the electric field direction, i.e.

$$\frac{\partial^2 f_1(x)}{\partial x^2} + \frac{1}{2E_{\|}} \frac{\partial V(x)}{\partial x} \frac{\partial f_1(x)}{\partial x} + \frac{2E_{\|}}{c^2\hbar^2}\big(\varepsilon - V(x)\big) f_1(x) = 0 \qquad (5.1)$$

for a spin directed along the longitudinal momentum, and

$$\frac{\partial^2 g(x)}{\partial x^2} + \frac{2E_{\|}}{c^2\hbar^2}\big(\varepsilon - V(x)\big) g(x) = 0 \qquad (5.2)$$

for a spin - opposite the longitudinal momentum. Here $E_{\|}$ is the longitudinal energy of a projectile, $E_{\|}^2 = p_{\|}^2 c^2 + mc^2$, $p_{\|}$ is the longitudinal momentum, mc^2 is the rest energy of projectile, ε is the energy of a bound state of the transverse motion, $V(x)$ is the potential energy, c is the speed of light, and $\hbar$ is the Planck constant. The function $f_1(x)$ in (5.1) is the 1st component of the 4-component Dirac spinor; and the function $g(x)$ in (5.2) is related with a 1st Dirac spinor

component by the expression

$$g(x) = \frac{1}{V(x) - \varepsilon} \frac{\partial f_1(x)}{\partial x}. \tag{5.3}$$

Obviously, one can use these results to consider the spin manifestation for channeling phenomena. Below only under-barrier states are taken into account.

5.1 Positron Channeling at Parabolic Potential Approach

The parabolic potential is a good approximation for interaction potential of positrons with crystal field near the center of plane channel between crystal planes; the positron potential energy can be presented as

$$V(x) = \frac{4U_0}{d^2} x^2, \tag{5.4}$$

U_0 is the depth of a potential well, and d is the distance between crystal planes.

Hence, Eqs.(5.1-5.2) for a positron should be written in the following

$$\frac{\partial^2 f_1(x_1)}{\partial x_1^2} + \frac{4U_0}{E_{\parallel}} x_1 \frac{\partial f_1(x_1)}{\partial x_1} + \frac{2E_{\parallel} d^2}{c^2\hbar^2}\left(\varepsilon - 4U_0 x_1^2\right) f_1(x_1) = 0, \tag{5.5}$$

$$\frac{\partial^2 g(x_1)}{\partial x_1^2} + \frac{2E_{\parallel} d^2}{c^2\hbar^2}\left(\varepsilon - 4U_0 x_1^2\right) g(x_1) = 0, \tag{5.6}$$

$x_1 = x/d$.

These equations have the solutions, which are written in terms of Hermitian's polynomials, and determine the spectrum of bound energy states [5.4]

$$\varepsilon_n^{\uparrow} = c\hbar(2n+1)\left(\frac{2U_0}{E_{\parallel} d^2}\left(1 + \frac{c^2\hbar^2 U_0}{2E_{\parallel}^3 d^2}\right)\right)^{1/2} + \frac{c^2\hbar^2 U_0}{E_{\parallel}^2 d^2} \tag{5.7}$$

for a spin along the longitudinal momentum of a plane, and

$$\varepsilon_n^{\downarrow} = c\hbar\left(\frac{2U_0}{E_{\parallel} d^2}\right)^{1/2}(2n+1) \tag{5.8}$$

for a spin opposite directed; n = 0, 1, 2, ...

As shown in [5.4], energy spectrum of ultra relativistic channeled particles in parabolic potential (5.4), when its spin is neglected, defined by the expression

$$\varepsilon_n = c\hbar\left(\frac{2U_0}{E_{\parallel} d^2}\right)^{1/2}(2n+1). \tag{5.9}$$

One can compare the distance between spin-related components of (5.7) and (5.8) with the distance between neighbor energy levels of spinless particle (5.9).

From (5.9) valid for spinless particles the distance between two neighbor levels n and n+1 is constant for every n and defined as

$$\Delta_n = \varepsilon_{n+1} - \varepsilon_n = 2c\hbar\left(\frac{2U_0}{E_{\|}d^2}\right)^{1/2}. \tag{5.10}$$

Presence of a spin results in the level splitting with a gap

$$\delta_n = \varepsilon_n^{\uparrow} - \varepsilon_n^{\downarrow} = c\hbar(2n+1)\left(\frac{2U_0}{E_{\|}d^2}\right)^{1/2}\left(\left(\frac{c^2\hbar^2U_0}{2E_{\|}^3d^2}+1\right)^{1/2}-1\right)+\frac{c^2\hbar^2U_0}{E_{\|}^2d^2}. \tag{5.11}$$

To evaluate the influence of a projectile spin to observable effects, let calculate the quantity δ_n/Δ_n:

$$\frac{\delta_n}{\Delta_n} = \left(n+\frac{1}{2}\right)\left(\left(\frac{c^2\hbar^2U_0}{2E_{\|}^3d^2}+1\right)^{1/2}-1\right)+\frac{c\hbar}{4E_{\|}}\left(\frac{2U_0}{E_{\|}d^2}\right)^{1/2} \tag{5.12}$$

If the quantity (5.12) is equal or almost equal to 1, the spin of a particle should be taken into account at simulation. And vice versa, if this quantity is rather small, $\delta_n/\Delta_n << 1$, the influence of a spin is negligible.

For estimations the depth of a potential well for planar channeling can be taken as $U_0 \approx 20$ eV, and the distance between atomic planes as $d \approx 2$ Å. Hence, the term $4U_0/d^2$ is about $2\cdot10^{17}$ eV/cm^2. It should be noticed that for relativistic energies $E_{\|} > 0.5$ MeV the quantity $c^2\hbar^2U_0/(2E_{\|}^3d^2) << 1$. Therefore, the 1st term in (5.12) can be considered as negligible small.

Moreover, it should be underlined, that the 1st term in (5.12), which includes the dependence on the level number n, may be indeed considered as zero. Successfully, the energy splitting is defined by the 2nd term of Eq. (5.12), i.e., it is constant for all energy levels at the fixed projectile energy $E_{\|}$.

Then, we obtain from (5.12):

$$\frac{\delta_n}{\Delta_n} \approx \frac{c\hbar}{4E_{\|}}\left(\frac{2U_0}{E_{\|}d^2}\right)^{1/2}. \tag{5.13}$$

The calculations are presented in Table 1. All estimates show that influence of a positron's spin can be omitted for considered projectile energy range $E_{\|} > mc^2 = 0.5$ MeV.

Longitudinal energy, MeV	Energy of the ground state of spinless particle ε_0, eV	The distance between spin-related components of ground state	δ_0 / Δ_0
0.6	8.1	5.4E-5	3.3E-6
5	2.8	7.8E-7	1.4E-7
50	0.9	7.8E-9	4.4E-9
500	0.3	7.8E-11	1.4E-10

Table 1. The spin-related characteristics of the electron channeling. The longitudinal polarization.

Above one obtained that for very wide range of projectile energies $E_{\|}$ the influence of a spin can be omitted. But this effect may be observable for some very specific crystals. For positron energy 500 MeV and typical crystals we have

$$\delta_0 / \Delta_0 \approx \frac{c\hbar}{4E_{\|}} \left(\frac{2U_0}{E_{\|} d^2} \right)^{1/2} \approx 10^{-10} \qquad (5.14)$$

If one would like to observe the effect for such a positron under planar channeling conditions that may correspond to the value of $\delta_0 / \Delta_0 \approx 0.05$, the coefficient $4U_0 / d^2$ should be equal 10^{31} eV/cm^2. This quantity requires both very deep potential well $U_0 > 1$ MeV and very small distances between crystal planes $d < 1$ pm. These parameters are rather distant from the parameters of existing crystals.

5.2 Electron Channeling at the Modified Poschle-Teller Potential

The modified Poschle-Teller potential is used as the simple approximation of the planar potential. The energy of interaction of projectile with the modified Poschle-Teller potential is:

$$V(x) = -U_0 \cosh^{-2}\left(x / b\right). \qquad (5.15)$$

U_0 is the depth of a potential well and b is the tabular parameter for given crystal planes. In our estimates parameter $b = a_x / 6$, a_x is the distance between crystal planes. In this case the crystal plane is located in the center of a channel considered. The bound states are formed for the transverse electron energies within the range $-U_0 < \varepsilon < 0$.

The equations (5.1), (5.2) in the case of potential energy (5.15) should be written as following:

$$\frac{\partial^2 f_1(x_1)}{\partial x_1^2} + \frac{U_0}{E_{\|}} \frac{\sinh(x_1)}{\cosh^3(x_1)} \frac{\partial f_1(x_1)}{\partial x_1} + \frac{2E_{\|} b^2}{c^2\hbar^2} \left(\varepsilon + \frac{U_0}{\cosh^2(x_1)} \right) f_1(x_1) = 0, \qquad (5.16)$$

$$\frac{\partial^2 g(x_1)}{\partial x_1^2} + \frac{2E_{\|} b^2}{c^2\hbar^2} \left(\varepsilon + \frac{U_0}{\cosh^2(x_1)} \right) g(x_1) = 0, \qquad (5.17)$$

$x_1 = x/b$. Eq.(5.17) has an analytical solution [5.5-5.6] while analytical solution of Eq.(5.17) is unknown.

The bound energy spectrum which is defined by Eq. (5.17) is [5.5]:

$$\varepsilon_n^{\downarrow} = -\frac{c^2\hbar^2}{2E_{\|}b^2}(s-n)^2, \text{ and } s = \frac{1}{2}\left(-1+\sqrt{1+\frac{8E_{\|}U_0b^2}{c^2\hbar^2}}\right). \tag{5.18}$$

The integer number n is changed from zero to the integer part of s. The wave functions for odd n $g_-(x_1)$ and for even n $g_+(x_1)$ are:

$$g_-(x_1) = \xi\left(1-\xi^2\right)^{\mu/2}\ {}_2F_1\left(\frac{\mu-s}{2}, \frac{\mu+s+1}{2}; \mu+1; 1-\xi^2\right), \tag{5.19}$$

$$g_+(x_1) = \xi\left(1-\xi^2\right)^{\mu/2}\ {}_2F_1\left(\frac{\mu-s+1}{2}, \frac{\mu+s+2}{2}; \mu+1; 1-\xi^2\right). \tag{5.20}$$

In Eqs. (5.19,5.20) $\xi = \tanh(x_1)$, $\mu_n = s-n$. The energies and corresponding parameters μ_n are related by expression

$$\varepsilon_n^{\downarrow} = -\frac{c^2\hbar^2}{2E_{\|}b^2}\mu_n^2. \tag{5.21}$$

In [5.4] it was shown that bound energy spectrum for the spinless particle is the same as one for the particle with the spin polarized opposite to the longitudinal momentum. As we assume that the influence of the projectile's spin is not strong, we can use the perturbation theory to obtain the approximated solution of eq. (5.16) from the solution of eq. (5.17). We apply the perturbation theory to find the approximated values of parameter μ^2 , as this parameter plays the role of "energy" in eq. (5.17).

The first correction to parameter μ_n^2 of the n-th energy level is defined by expression:

$$\delta\left(\mu_n^2\right) = \frac{U_0}{E_{\|}}\int g_n(x_1)\frac{\sinh(x_1)}{\cosh^3(x_1)}\frac{\partial g_n(x_1)}{\partial x_1}dx_1 . \tag{5.22}$$

We can use the Eq. (5.21) to obtain the energies of projectile, which has the spin polarized along the longitudinal momentum:

$$\varepsilon_n^{\uparrow} = \varepsilon_n^{\downarrow} - \frac{c^2\hbar^2}{2E_{\|}b^2}\delta\left(\mu_n^2\right). \tag{5.23}$$

The distance between spin-related components of n-th energy level is

$$\delta_n = \varepsilon_n^{\uparrow} - \varepsilon_n^{\downarrow} = -\frac{c^2\hbar^2}{2E_{||}^2 b^2}\delta\left(\mu_n^2\right). \tag{5.24}$$

One can compare the distance between spin-related components of (5.24) with the distance between neighbor energy levels of spinless particle (5.21) $\Delta_n = \varepsilon_{n+1} - \varepsilon_n$. The numerical estimations are carried out at $U_0 \approx 20$ eV and $d \approx 2$ Å. These estimations are presented in Table 2 and show, that the influence of the electron's spin is the negligible.

Number of level n	Energy of spinless particle ε_n, eV	The distance between spin-related components δ_n, eV	δ_n / Δ_n
Electron energy $E_{||} = 0.6$ MeV			
0	-6.3	6.0E-5	-
Electron energy $E_{||} = 5$ MeV			
0	-13.2	3.1E-6	3.1E-7
1	-3.1	-8.6E-7	-
Electron energy $E_{||} = 50$ MeV			
0	-17.5	5.4E-8	1.2E-8
1	-12.9	2.7E-8	6.8E-9
2	-9.0	8.3E-9	2.6E-9
3	-5.8	-1.1E-8	-4.6E-9
Electron energy $E_{||} = 500$ MeV			
0	-19.2	6.5E-10	4.0E-10
1	-17.6	5.4E-10	3.5E-10
2	-16.0	4.4E-10	3.0E-10
3	-14.6	3.0E-10	2.2E-10

Table 2. The spin-related characteristics of the electron channeling. The longitudinal polarization.

5.3 Discussions and Conclusions

Above we found that the account of the longitudinal polarization manifests at splitting every energy levels into two sublevels that correspond two possible spin projections onto the longitudinal momentum. The distance between spin-related sublevels is very small in comparison with the interval between neighboring levels of spinless channeled particle. In principle, one could observe two lines (with small shift) in radiation spectra of particles.

Now we estimate this shift in laboratory frame, when the Doppler Effect is taken into account. The energy gap between lines in the laboratory frame is defined by expression:

$$\delta_{Dop} = \frac{\delta}{1 - \beta\cos\theta}. \tag{5.25}$$

Let $\beta = v/c$ and δ are fixed. The gap δ_{Dop} is the largest if the angle between projectile

velocity *v* and the direction of observation is $\theta = 0$.

The best conditions to observe the spin-related splitting of the lines are at $E_{||} = 0.6\,\mathrm{MeV}$ ($\beta = 0.52$) and $\delta = 5.4\,\mathrm{E}-5$ for positrons. Hence, the gap between lines is $\delta_{Dop} = 0.00011$ eV (i.e. 0.89 cm^{-1}). Analogous, for electrons from (5.25) and Table 2, one obtain $E_{||} = 0.6\,\mathrm{MeV}$, $\beta = 0.52$, $\delta = 6\,\mathrm{E}-5$, and $\delta_{Dop} = 0.00012$ eV (i.e. 0.97 cm^{-1}).

Therefore, the even modern experimental equipment does not able to separate these lines. Moreover, the broadening of levels from amount causes must prevent to observe the "fine structure" of energy levels near the peak of potential well.

6. LNF EXPERIMENTAL FACILITIES FOR PERSPECTIVE CRYSTAL-ASSISTED EXPERIMENTS

All the details of LNF accelerator facilities (SPARC/SPARX and DAΦNE BTF) are well presented by many reports publications (see, for instance, [6.1,6.2])

The overall SPARC (Sorgente Pulsata Auto-amplificata di Radiazione Coerente) [6.3] project consists of 4 main lines of activity aiming at several goals: their common denominator is to explore the scientific and technological issues that set up the most crucial challenges on the way to the realization of a SASE-FEL based X-ray source, the SPARX proposal [6.4] ((Fig. 6.1)).

These are:

- 150 MeV Advanced Photo-Injector;
- SASE-FEL Visible-VUV Experiment;
- X-ray Optics/Monochromators;
- Soft X-ray table-top Source.

Since the performances of X-ray SASE-FEL's are critically dependent on the peak brightness of the electron beam delivered at the undulator entrance, investigations have been performing for two main issues - generation of the electron beam and bunch compression via magnetic and/or RF velocity bunching - by means of an advanced system delivering 150 MeV electrons, the minimum energy to avoid further emittance dilutions due to the time dependent space charge effects.

In order to study the problems related to matching the beam into an undulator and keeping it well aligned to the radiation beam, as well as the generation of non-linear coherent higher harmonics, a SASE FEL experiment with the 150 MeV beam, using a segmented undulator with additional strong focusing, will be organized to observe FEL radiation at 530 nm and below. The X-ray FEL radiation will provide unique radiation beams to users in terms of peak brightness and pulse time duration (100 fs), posing at the same time severe challenges to the optics that is necessary to guide and handle such radiation. This project is pursuing also a vigorous R&D activity on the analysis of radiation-matter interactions in the spectral range typical of SASE X-ray FEL's (from 0.1 to 10 nm), as well as the design of new optics and monochromators compatible with these beams. In order to test these optics and to start the R&D on applications, the project undertakes an upgrade of the presently operated table-top source of X-rays at Politecnico Milano, delivering 107 soft X-ray photons in 10-20 fs pulses by means of high harmonic generation in a gas.

SPARX source ability to deliver an enormous amount of energy on small areas will make possible to study effects that, up to now, can only be theoretically predicted. In particular interesting results are expected in the field of photochemistry, with important industrial

applications. High peak brightness and short pulse duration (a few fs) will be the main characteristics of the SPARX source. By using a 2.5 GeV linear electron accelerator and two magnetic undulators it is possible to obtain radiation at 10 nm and 1.5 nm. Exploitation of 3rd and 5th harmonics will allow emission in the range between 10 and 2 nm for the first beam line and between 1.5 and 0.3 nm for the second beam line. The aim of the PLASMON-X project [6.5] is to provide the LNF with a world-class, high-power laser facility suitable for the development of an innovative, high gradient acceleration technique based upon super-intense and ultra-short laser pulses, and X/γ-ray tunable sources using Thomson scattering of optical photons by energetic electrons. The facility will be built in close interaction with the SPARC project presently in progress.

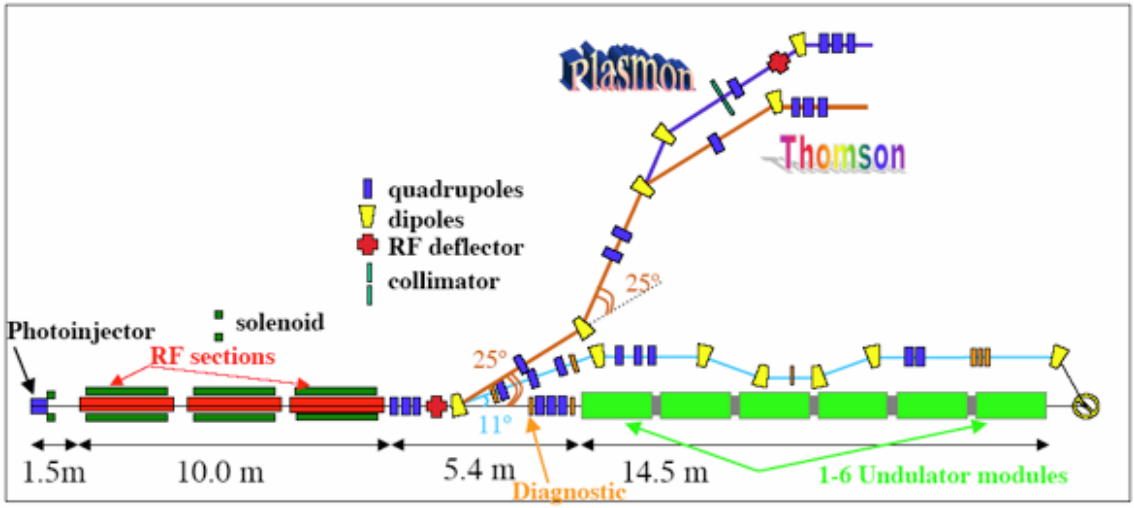

Figure 6.1. Scheme of SPARC layout.

The DAΦNE Beam Test Facility is operating since 2002 providing electrons and positrons from the single particle up to 10^{10}particles per a spill and from 20 to 800 MeV (750 MeV for positrons) [6.6, 6.7]. The positron beam with a maximum energy of 750 MeV, provided by the DAΦNE BTF has shown to be the ideal tool to test this novel idea. The BTF can also provide photons of well tagged energy thanks to a system composed of a silicon tracking chamber (made of up 4 layers of single-sided micro-strips), placed at the inlet of the final bending magnet, and of silicon single-sided micro-strip detectors covering the inner wall of the vacuum chamber inside the dipole. The particles hitting the chambers produce photons by bremsstrahlung and according the position where the particles impinge on the dipole wall it is possible to define the energy of the emitted photons.

Last years, the facility has hosted several tens of high energy tests and experiments from all Europe, satisfying requests to operate in a very wide range of beam intensity and energy. The main applications of the facility have been: high energy detector calibration, low energy calorimetry, low energy electromagnetic interaction studies, detector efficiency and aging measurements, test of beam diagnostic devices, etc. A 100 square meters area, fully equipped with diagnostic and Data Acquisition systems, is available for hosting experiments.

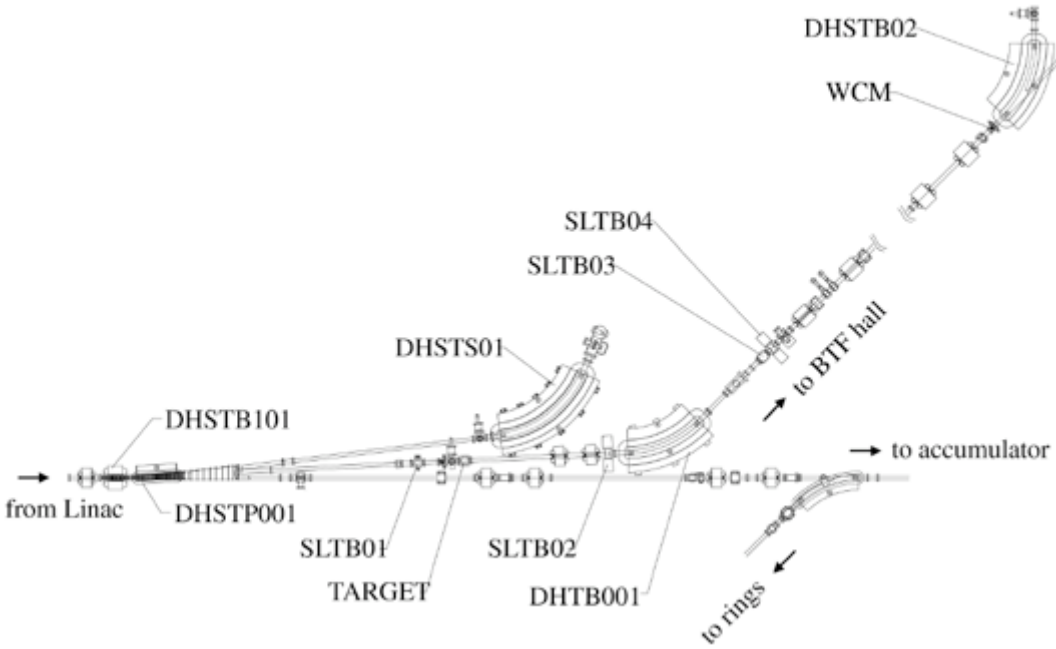

Figure 6.2. BTF beamlines layout.

Thanks to a pulsed dipole magnet, that has been installed at the end of LINAC during the DAΦNE shutdown in June 2006, the BTF received continuously beam in its experimental area, allowing the users to take data, even during the injection in the DAΦNE rings (up to 90% of duty cycle respect to the overall Linac working time).

The DAΦNE-BTF seems to be the unique European facility that can deliver positron beams in the range of energy required for the CUP experiment (Crystal Undulator for Positrons, INFN Gr.V). In fact, according to well-accepted channeling radiation theories, a strong photon peak at MeV-energies should appear for planar channeling in a monocrystal at positron beam energy of about 600 MeV. At the BTF, this peak should be detected and its intensity should be investigated as a function of crystal thickness, angle of incidence, etc. From these first measurements, the very important dechanneling length can be determined and both dechanneling and rechanneling processes be deeply studied.

REFERENCES

Section 1:

1. M.Ter–Mikaelian, *Zh.Eksp.Teor.Fiz.* **25** (1953) 296.
2. H.Uberall, *Phys.Rev*. **103**, (1956), 1055.
3. G. Bologna, G. Diambrini Palazzi, and G. P. Murtas, *Phys. Rev. Letters* **4** (1960) 34.
4. P.G.Diambrini, *Rev.Mod.Phys*. **10**, (1968), 611.
5. M.Ter–Mikaelian, *High Energy Electromagnetic Processes in Condensed Media*, Wiley, New–York, 1972.
6. N.Cue and J.C.Kimball, *Phys. Lett*. **124**, (1987), 191.
7. R.O.Avakyan, A.E.Avetisyan, V.A.Gurdjsn, *et al.*, *Pis'ma Zh.Eksp.Teor.Fiz*., **51**, (1990), 627.
8. M. Andreyashkin, A. B. Basai, S. A. Vorobiev, V.N.Zabaev, B.N.Kalinin, Yu.P.Kunashenko, Yu.L.Pivovarov. *Pis'ma Zh.Eksp.Teor.Fiz*., **55**, (1992),407 .

9. Yu.P.Kunashenko and Yu.L.Pivovarov, *Nucl.Instr.Meth.* **B114**, (1996), 237.
10. Yu.P.Kunashenko and Yu.L.Pivovarov, *Nucl.Instr.Meth*. **B115**, (1996), 390.
11. Yu.P.Kunashenko and Yu.L.Pivovarov, *Nucl.Instr.Meth.* **B145**, (1998), 106.
12. Y.Okazaki, M.Andreyashkin, K.Chouffani, I.Endo, R.Hamatsu, M.Iinuma, H.Kojima, Yu.P.Kunashenko, M.Masuyama, T.Ohnishi, H.Okuno, Yu.L.Pivovarov, T.Takahashi, Y.Takashima. *Phys.Lett*. **A271,** (2000), 110.
13. I.Endo, Y.Okazaki, Yu.P.Kunashenko, Yu.L.Pivovarov. *Nucl.Instr.Meth.* **B179,** (2001), 343.
14. G.V.Meledin, V.G. Serbo and A.K. Slivkov, *JETP Letters* , **13,** (1971), 68.
15. H.A.Olsen, *Phys. Rev*. **D33**, (1986), 2033.
16. V.L.Lyuboshits, *Yad. Fiz.* **45,** (1987), 682.
17. E.Holvik, H.A.Olsen, *Phys.Rev*. **D35,** (1987), 2124.
18. S.Gevorkyan, E.Kuraev, A.Tarasov, A.Shilleer, V.G.Serbo. Workshop "Hadronic atoms and positronium in the standard model", eds. M.A. Ivanov, E.A. Kuraev,E2-98-254, Dubna (1998) 183.
19. S.Gevorkyan, E.Kuraev, A.Schiller, V.G.Serbo, A.Tarasov. *Phys.Rev*. **A58,** (1998) 1556.
20. G.L.Kotkin, E.A.Kuraev, A.Schiller, V.G.Serbo, A.Tarasov. *Phys.Rev.* **C59,** (1999), 2734.
21. H.A.Olsen, *Phys. Rev.* **A63,** (2001), 032101.
22. H.A.Olsen, *Phys. Rev.* **A60**, (1999) 1883.
23. Yu.P.Kunashenko, Yu.L.Pivovarov, *Sov. J. Nucl. Phys.* **V.51, Issue 3,** (1990), 397.
24. G.I.Sandnes, H.A.Olsen, *Phys. Rev.* **A48,** (1993), 3725.
25. Yu.P. Kunashenko and Yu.L. Pivovarov, *Nucl.Instr.Meth.* **B114,** (1996), 237. *Nucl.Instr.Meth.* B119, **(1996), 137.**
26. Yu.L.Pivovarov, Yu.P. Kunashenko, I. Endo, T. Isshiki, *Nucl.Instr.Meth.* **B145,** (1998), 80.
27. Yu.P. Kunashenko, *Nucl.Instr.Meth.* **B229,** (2005), 219.
28. Workshop "Hadronic atoms and positronium in the standard model", eds. M.A. Ivanov, E.A. Kuraev, E2-98-254, Dubna 1998.

Section 2:

1. V. N. Baier, V. M. Katkov, V. M. Strakhovenko, *Electromagnetic Processes at High Energies in Oriented Single Crystals*, World Scientific Publishing Co, Singapore, 1998.
2. V.G. Bagrov, G.S. Bisnovatiy-Kogan, V.A. Borodovitsyn, A.V. Borisov, O.F. Dorofeev, V.Ch. Zhukovskiy,Yu.L.Pivovarov, O.V. Shorokhov, and V.Ya. Epp, *Theory of Radiation of Relativistic Particles*, (FizMatLit., Moscow, 2002) (in Russian).
3. M.A.Kumakhov, *Radiation of Channeled Particles in Crystals* (Energoatomizdat, Moscow) 1986 (in Russian); Radiation from Charged Particles in Solids (AIP Translation S.) by M.A. Kumakhov, F.F. Komarov, and G. Kurizki (Hardcover - April 1993)
4. O.V. Bogdanov, K.B. Korotchenko, Yu.L. Pivovarov, *J. Phys. B*. **41** 055004 (2008)
5. V.V. Denyak, I.G. Evseev, V.M. Khvastunov, V.P. Likhachev, S.A. Paschuk, H.R. Schelin. *Braz. J. Phys.* vol.33 no.1 Sro Paulo Mar. 2003
6. S.A. Vorobyov, E.G. Vyatkin, Yu.L. Pivovarov, A.P. Potylitsyn, and I. Khakberdiyev, *JEThP*. **94**, 38 (1988).

Section 3:

1. V.G. Baryshevsky and I.Ya. Dubovskaya, *J. Phys.* C **16**, 3663 (1983).
2. T.Ikeda, Y.Matsuda, H.Nitta, Y.H.Ohtsuki. *Nuclear Instruments & Methods in Physics Research* **B115** (1996) 380-383
3. Y.Matsuda, T.Ikeda, H.Nitta, H.Minowa, Y.H.Ohtsuki. *Nuclear Instruments & Methods in Physics Research* **B115** (1996) 396-400

4. R.Yabuki, H.Nitta, T.Ikeda, Y.H.Ohtsuki. *Physical Review* B, V.**63**, 174112 (2001)
5. O.V. Bogdanov, K.B. Korotchenko, Yu.L. Pivovarov, *JETP Letters.* V. **85**, 11, 555 (2007)
6. K.B. Korotchenko, Yu.L. Pivovarov, T.A. Tukhfatullin, *Instr. Meth.* **B** doi: 10.1016/j.nimb.2008.03.203

Section 4:

1. A.I.Akhiezer, and N.F. Shu'lga, High Energy Electrodynamics In Matter, Gordon and Breach, Luxemburg, 1996.
2. V.A.Dolgikh, Yu.P.Kunashenko, and Yu.L. Pivovarov, *Nucl. Instr. Meth.* **B201** (2003) 253.
3. V.I.Efremov, and Yu.L.Pivovarov. Proceedings of International Conference on Charged and Neutral Particles Channeling phenomena II: "Channeling 2006", *Proc. SPIE* **6634** (2006) 66340T.
4. V.I. Efremov, V.A.Dolgikh, Yu.L. Pivovarov, *Izvestia VUZov. Fizika*. V.**50** 12, 61 (2007)
5. Review of Particle Physics. *Physical Review* D **54**(1) (1996) 134.

Section 5:

1. L.D. Landau, and E.M. Lifshits *Theoretical Physics. Quantum Electrodynamics*, chapters 3,4, Fizmatlit, Moscow, 2001 (in Russian).
2. M.A. Kumakhov, *Radiation from Channeled Particles in Crystals*, Energoatomizdat, 1986 (in Russian).
3. J. Augustin, A. Shafer, W. Greiner. *Phys. Rev.* A. **51**, 2 (1995) 1367.
4. A. Babaev, *Proc. of SPIE*, **6634** (2007) 66340A.
5. V. V. Lasukov, Yu. L. Pivovarov, O. G. Kostareva, *Phys. Stat. Sol.* (b), **109** (1982) 761.
6. S. Flugge. *Practical Quantum Mechanics*, vol. 1., Springer-Verlag, Berlin, Heidelberg, New York, 1971.

Section 6:

1. Proceedings of International Conference on Charged and Neutral Particles Channeling Phenomena I: "Channeling 2004" (Frascati, 2-6 November, 2004), *Proc. SPIE* **5974 (**2005**);** Proceedings of International Conference on Charged and Neutral Particles Channeling Phenomena II: "Channeling 2006" (Frascati, 3-7 July, 2006), *Proc. SPIE* **6634 (**2007**);**
2. Proceedings of International Conference "The Physics and Applications of High Brightness Electron Beams" (Erice, 10-15 October 2005), World Scientific, 2007.
3. D. Alesini et al. "Status of the SPARC Project", presented at **PAC2005** 16-20/5/2005, Knoxville, Tennessee, USA.
4. http://www.sparx.it/
5. http://ilil.ipcf.cnr.it/plasmonx
6. G. Mazzitelli, A. Ghigo, F. Sannibale, P. Valente, G. Vignola, *Nucl. Instr. Meth. in Phys. Res.* **A 515** (2003) 524-542
7. M. Anelli, B. Buonomo, G. Mazzitelli and P. Valente, Preprint **LNF-04/24 (IR)** - 15 Nov. 2004.